Structural optimization under overhang constraints imposed by additive manufacturing technologies

Grégoire Allaire, Charles Dapogny, Rafael Estevez, Alexis Faure, Georgios Michailidis

STRUCTURAL OPTIMIZATION UNDER OVERHANG CONSTRAINTS IMPOSED BY ADDITIVE MANUFACTURING TECHNOLOGIES

G. ALLAIRE[1], C. DAPOGNY[2], R. ESTEVEZ[3], A. FAURE[3], AND G. MICHAILIDIS[3]

[1] *Centre de Mathématiques Appliquées, Ecole Polytechnique, CNRS, Université Paris-Saclay, 91128 Palaiseau, France*
[2] *Laboratoire Jean Kuntzmann, Université Grenoble-Alpes, CNRS, Grenoble INP, F-38000, France*
[3] *SIMaP, Université Grenoble-Alpes, CNRS, Grenoble INP, F-38000, France*

Abstract. This article addresses one of the major constraints imposed by additive manufacturing processes on shape optimization problems - that of overhangs, i.e. large regions hanging over void without sufficient support from the lower structure. After revisiting the 'classical' geometric criteria used in the literature, based on the angle between the structural boundary and the build direction, we propose a new mechanical constraint functional, which mimics the layer by layer construction process featured by additive manufacturing technologies, and thereby appeals to the physical origin of the difficulties caused by overhangs. This constraint, as well as some variants, are precisely defined; their shape derivatives are computed in the sense of Hadamard's method and numerical strategies are extensively discussed, in two and three space dimensions, to efficiently deal with the appearance of overhang features in the course of shape optimization processes.

Contents

1. Introduction

The recent breakthroughs in the development of additive manufacturing technologies have given a new impetus to the capabilities of construction processes. Their unique potential as regards the complexity of the assembled designs is no longer restricted to their original purpose of rapid prototyping, and they have already been integrated into various real-life, industrial environments; as an illustration, additive manufacturing

technologies have been used in the automotive industry [13], in biomedical engineering [27], etc; see [37] for an overview.

Let us present shortly the main features of additive manufacturing techniques, referring to [6, 20] and the introduction in [12] for more detailed accounts. Additive manufacturing is a common label for quite different construction processes, all of which starting by a slicing operation: the Computer Aided Design (CAD) model for the input shape (which is often supplied under the form of a surface mesh) is converted into a series of two-dimensional layers; see Figure 1. Thence, these layers are assembled individually, one

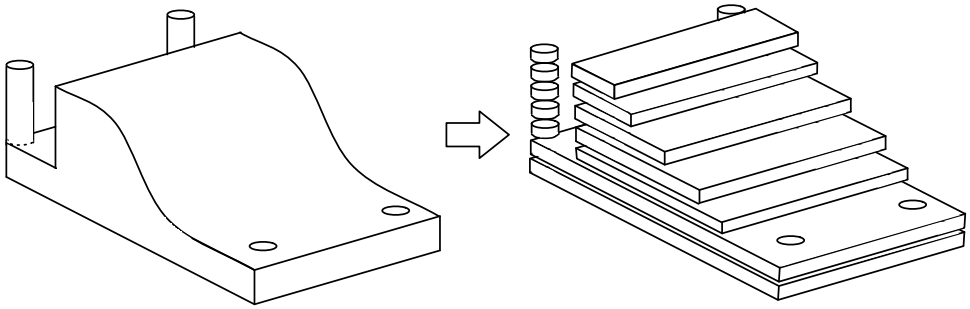

FIGURE 1. *Rough sketch of the slicing procedure, initiating any additive manufacturing process.*

above the other, according to the particular technology at play.

These technologies show competing features as far as their speed, cost, accuracy, and the nature of the processed materials are concerned. Two important categories are the following (see Figure 2 for illustrations):

- Material extrusion methods, such as Fused Filament Fabrication (FFF), use a nozzle to extrude the molten material, which is then deposited into rasters; such methods are typically used to process thermoplastics (ABS), although recent studies have considered applying the same principle with metal [29].
- Powder bed fusion strategies (such as Selective Laser Melting, or Electron Beam Melting) are generally used to process metal; at the beginning of the construction of each layer, metallic powder is spread within the build chamber and a laser (or an electron beam) is used to bind the grains together.

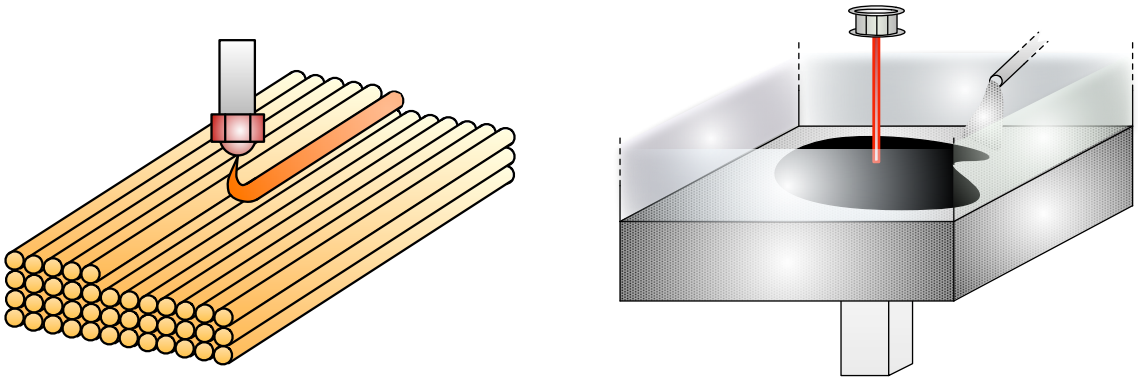

FIGURE 2. *(Left) Sketch of Fused Filament Fabrication methods: a molten filament is deposited by a nozzle along rasters; (right) sketch of the Electron Beam Melting technology: metallic powder is fused by an electron beam, giving birth to the desired shape.*

In spite of their unique assets, additive manufacturing technologies also suffer from major drawbacks when compared to traditional construction methodologies: at first, they are not scalable, contrary to, for instance,

casting techniques where the mold, once it is constructed, can serve to produce quickly and efficiently thousands of copies of the desired component. What's more, because of the specific path followed by the printing nozzle or laser, the material properties of parts produced by additive manufacturing methods are not precisely controlled, and many ongoing studies aim at quantifying the induced anisotropic behavior; see for instance [1, 46].

On a different note, closer to the topic of the present article is the difficulty experienced by almost all additive manufacturing techniques when it comes to building parts showing large *overhangs*, that is large features close to horizontal, hanging over void, without sufficient support from the lower structure; see Figure 3 for an illustration. Beyond the increased staircase effect entailed by the assembly of such regions, the reason for this difficulty varies from one additive manufacturing technology to the other:

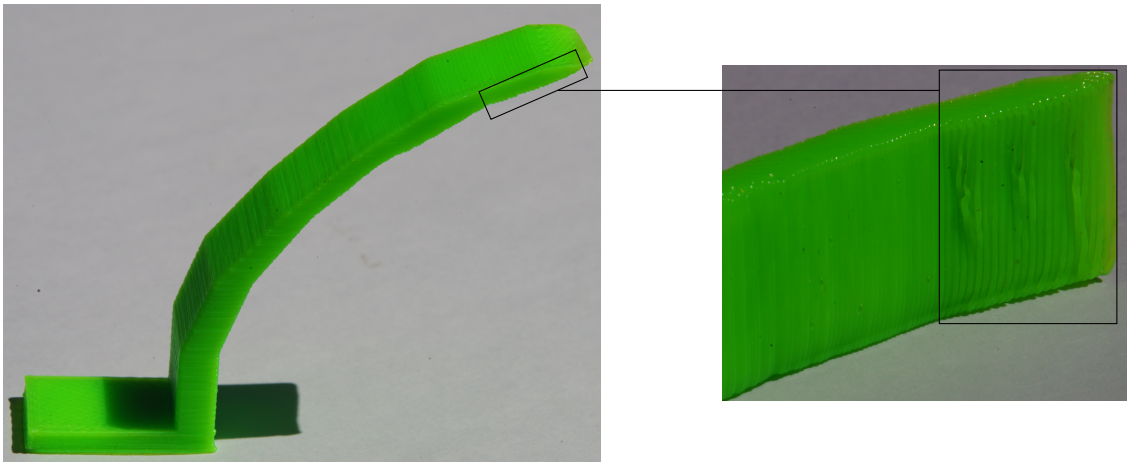

FIGURE 3. *The angle between the structural boundary and the build direction has a direct impact on the quality of the processed shape.*

- In the case of material extrusion methods, structures with large overhangs cannot be produced as is, since this demands depositing material on void.
- In the case of powder bed fusion methods, the rapid melting then solidification of the material induces large thermal variations in the structure; this creates residual stresses, and eventually causes warpage. This phenomenon is all the more likely to occur in regions which are unanchored to the lower structure (in particular, overhanging regions); see [31]. Another source of difficulties in the assembly of overhanging regions lies in that the fused material may drip between the unfused powder of the lower structure, thus leaving the processed boundary with rough patches [10].

Several possibilities have been thought off to deal with the presence of overhangs in the constructed shapes. Most of them are post-processing methods, i.e. they apply to the final shape (and they are not included in the prior design optimization stage). In this direction, much effort has been devoted to the construction of an efficient *scaffold structure* to support the shape, which has to be removed at the end of the process; see for instance [16]. Other works have focused on identifying the best build direction, which minimizes the volume of the needed support structure, or the impact of the staircase effect on the cylindricity and flatness errors [15, 36]. Let us eventually mention the works [9, 23, 26] in which the constructed design is modified so that it becomes self-supporting.

On the contrary, surprisingly few works tackle the penalization of overhangs at the level of the shape optimization problem. As far as this strategy is concerned, most investigations focus on criteria based on the angle between the structural boundary and the build direction. In [8], a quite complicated procedure is proposed which is based on the average angle between every overhanging region and the build direction, but the sensitivity analysis of the resulting criterion is postponed to a further publication and no actual implementation of the method is reported. In [19], a filter is introduced for density-based topology optimization, whereby the value of the density field at each point depends on those in the lower regions which are eligible to provide support to the considered point; a quite similar approach is used in the works [24, 25]. In [39],

still in the context of density-based topology optimization, the problem is formulated as the penalization of the angle between the gradient of the density function and the build direction. In the interesting work [30], an optimization algorithm is proposed to optimize at the same time the shape and the amount of material needed for the supporting scaffold structure during its assembly. This procedure relies on the topological sensitivity analysis of the latter quantity. Last but not least, from a quite different point of view, the contribution [44] aims at extracting a self-supporting truss structure from a continuous shape, composed of a minimum amount of material.

The main goal of the present article is to explore two alternative strategies for constraining the presence of overhangs in shape and topology optimization problems. On the one hand, we address the problem in a purely geometric manner, which is reminiscent of the aforementionned angle-based criteria used in the literature. On the other hand, we use a new formulation which takes advantage of the theoretical background developed in our previous work [3], and appeals to the mechanical origin of the difficulty to build overhangs. More precisely, we propose a new constraint functional which is based on a simplified model for the manufacturing process: we distinguish between the *final* shape, which is the end component used in the real-life context (this is the shape whose mechanical performance is evaluated and optimized), and the *intermediate* shapes Ω_h, corresponding to snapshots taken during the construction process of Ω, where Ω has been assembled layer by layer, up to height h. The physical behavior of the Ω_h during the manufacturing stage is modelled, and aggregated into a single constraint functional. We present several numerical investigations about the respective achievements of both formulations, and we infer efficient numerical strategies to deal with the presence of overhangs in the produced shapes.

The remainder of this article is organized as follows. In Section 2, we present the shape optimization problem at stake, namely that of compliance minimization, and we recall some classical notions about shape derivatives. In Section 3, we introduce geometric shape functionals which rely on the angle between the structural boundary and the build direction to constrain the presence of overhangs in shape optimization problems. Section 4 is devoted to the description, analysis and implementation of a mechanical constraint functional (and variants of it) to achieve this goal. Eventually, in Section 5, we discuss several numerical instances of shape optimization problems under overhang constraints and we appraise the efficiency of the proposed formulations.

2. Shape optimization of linearly elastic structures

2.1. Description of the shape optimization problem.

The objects in the place of honor in this article are *shapes*, that is, bounded domains $\Omega \subset \mathbb{R}^d$, filled with a linear elastic material characterized by its Hooke's tensor A. Each shape Ω is clamped on a subset Γ_D of its boundary, and is submitted to surface loads $f \in L^2(\Gamma_N)^d$ applied on a subset Γ_N of $\partial\Omega$ which is disjoint from Γ_D. The complementary region $\Gamma := \partial\Omega \setminus (\overline{\Gamma_D} \cup \overline{\Gamma_N})$ is traction-free. For later purpose (see Section 4), we introduce an additional, non optimizable subset Γ_0 of $\partial\Omega$ which may overlap Γ_D, Γ_N or Γ.

In the context of its *final* (i.e. practical) utilization, the physical behavior of a shape Ω is described by the elastic displacement u_Ω, which is the unique solution in the space

$$H^1_{\Gamma_D}(\Omega)^d := \left\{ u \in H^1(\Omega)^d, \;\; u = 0 \text{ on } \Gamma_D \right\}$$

to the *mechanical* system:

$$\left\{ \begin{array}{cl} -\mathrm{div}(Ae(u_\Omega)) = 0 & \text{in } \Omega, \\ u_\Omega = 0 & \text{on } \Gamma_D, \\ Ae(u_\Omega)n = 0 & \text{on } \Gamma, \\ Ae(u_\Omega)n = f & \text{on } \Gamma_N. \end{array} \right. \tag{2.1}$$

In the above system, $e(u) := \frac{1}{2}(\nabla u + \nabla u^T)$ is the (linearized) strain tensor associated to the displacement u, and n (or equivalently n_Ω when it comes to emphasizing its dependence on Ω) denotes the unit normal vector to $\partial\Omega$, pointing outward Ω.

Without loss of generality, in the present article, the mechanical performance of Ω is evaluated in terms of its (structural) compliance

$$J(\Omega) = \int_\Omega Ae(u_\Omega) : e(u_\Omega)\, dx = \int_{\Gamma_N} f \cdot u_\Omega\, ds, \tag{2.2}$$

as a measure of the elastic energy stored in Ω during its deformation, or equivalently of the work of the external loads acting on it; see for instance [5, 7] for other possible objective functions. This criterion is minimized among the set $\mathcal{U}_{\rm ad}$ of admissible shapes defined by:

$$\mathcal{U}_{\rm ad} := \left\{\Omega \subset \mathbb{R}^d \text{ is smooth and bounded, } \Gamma_D \cup \Gamma_N \cup \Gamma_0 \subset \partial\Omega\right\}.$$

So that the shape optimization problem be physically relevant, we shall impose constraints, modelled by one (or several) function $P(\Omega)$ of the domain. Simple examples as for $P(\Omega)$ are the volume $\mathrm{Vol}(\Omega)$ and perimeter $\mathrm{Per}(\Omega)$ of shapes, which are respectively defined by:

$$\mathrm{Vol}(\Omega) = \int_\Omega dx, \text{ and } \mathrm{Per}(\Omega) = \int_{\partial\Omega} ds; \tag{2.3}$$

the main purpose of this article is to devise other constraint functionals enforcing the constructibility of shapes by additive manufacturing technologies.

In the present work, we rely on two different strategies to incorporate a generic constraint $P(\Omega)$ into the optimization process; on the one hand, we consider unconstrained problems, of the form:

$$\min_{\Omega\in\mathcal{U}_{\rm ad}} J(\Omega) + \ell P(\Omega), \tag{2.4}$$

where ℓ is a given penalization parameter. On the other hand, we may alternatively formulate the problem in the language of constrained optimization:

$$\min_{\Omega\in\mathcal{U}_{\rm ad}} J(\Omega) \text{ such that } P(\Omega) \le \alpha, \tag{2.5}$$

where α is a maximum imposed value for $P(\Omega)$.

2.2. **Shape sensitivity using Hadamard's boundary variation method.**

Most numerical algorithms dealing with unconstrained or constrained optimization problems of the form (2.4) or (2.5) are based on the derivatives of the objective and constraint functionals $J(\Omega)$ and $P(\Omega)$. In the shape optimization context, the usual notion of differentiation with respect to the domain is provided by Hadamard's boundary variation method [2, 32, 38]. In this setting, variations of a domain $\Omega \subset \mathbb{R}^d$ are considered under the form:

$$\Omega_\theta := (\mathrm{Id} + \theta)(\Omega),\ \ \theta \in W^{1,\infty}(\mathbb{R}^d, \mathbb{R}^d),\ \ ||\theta||_{W^{1,\infty}(\mathbb{R}^d,\mathbb{R}^d)} < 1; \tag{2.6}$$

see Figure 4.

Accordingly, a function $F(\Omega)$ of the domain is *shape differentiable* at Ω if the underlying mapping $\theta \mapsto F(\Omega_\theta)$, from $W^{1,\infty}(\mathbb{R}^d, \mathbb{R}^d)$ into $\mathbb{R}$ is Fréchet differentiable at 0; the corresponding derivative is denoted by $F'(\Omega)$ and the following asymptotic expansion holds, in the neighborhood of 0:

$$F(\Omega_\theta) = F(\Omega) + F'(\Omega)(\theta) + o(\theta), \text{ where } \frac{|o(\theta)|}{||\theta||_{W^{1,\infty}(\mathbb{R}^d,\mathbb{R}^d)}} \xrightarrow{\theta\to 0} 0.$$

In practice, shape deformations θ are often restricted to a subset of $W^{1,\infty}(\mathbb{R}^d, \mathbb{R}^d)$ composed of admissible variations; in the present work, we consider the sets:

$$\Theta^k := \left\{\theta : \mathbb{R}^d \to \mathbb{R}^d \text{ is } k \text{ times continuously differentiable and bounded, } \theta = 0 \text{ on } \Gamma_D \cup \Gamma_N \cup \Gamma_0\right\}.$$

For instance, it is well-known (see e.g. [5, 22]) that the functions $\mathrm{Vol}(\Omega)$, $\mathrm{Per}(\Omega)$ and $J(\Omega)$ defined by (2.3) and (2.2) respectively are shape differentiable for deformations $\theta \in \Theta^k$ ($k \ge 1$), and that:

$$\mathrm{Vol}'(\Omega)(\theta) = \int_\Gamma \theta \cdot n\, ds, \quad \mathrm{Per}'(\Omega)(\theta) = \int_\Gamma \kappa\, \theta \cdot n\, ds,$$

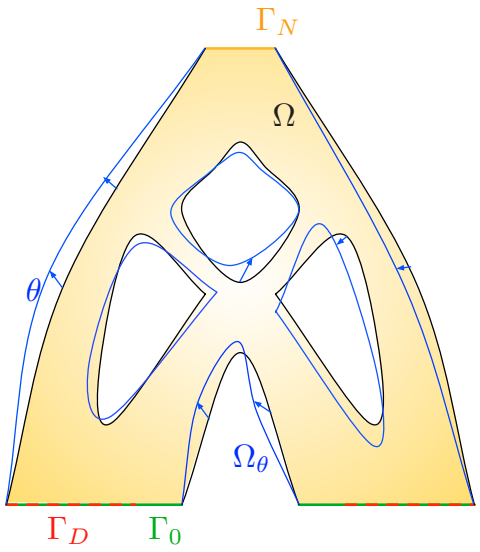

FIGURE 4. *One variation Ω_θ of an admisible shape Ω.*

where $\kappa : \partial\Omega \to \mathbb{R}$ is the mean curvature of $\partial\Omega$, and:

$$J'(\Omega)(\theta) = -\int_\Gamma Ae(u_\Omega) : e(u_\Omega)\, \theta \cdot n\, ds.$$

3. Geometric constraint functionals

As we have mentioned in the introduction, the prevalent quantity used in the literature to detect and constrain the presence of overhangs is the angle between the normal vector n_Ω to the structural boundary $\partial\Omega$ and the negative build direction $-e_d$, where e_d is th d^{rh} vector in the canonical basis of $\mathbb{R}^d$. This relies on the generally accepted heuristic that most additive manufacturing tools experience trouble in building features where this angle is lower than a certain threshold - the value 45° is often found in the literature; see e.g. [42].

In this section, we formulate geometric constraints based on this criterion, borrowing some material introduced in another context (that of architectural design) in [14]. We consider *anisotropic perimeter* functionals of the form:

$$P_g(\Omega) = \int_{\partial\Omega} \varphi(n_\Omega)\, ds, \tag{3.1}$$

where $\varphi : \mathbb{R}^d \to \mathbb{R}$ is a given function of class $\mathcal{C}^1$. Two particular instances of such functions φ will come in handy:

- The choice

$$\varphi_a(n) := (n \cdot e_d + \cos\nu)_-^2, \text{ where } (s)_- := \min(s, 0), \tag{3.2}$$

  and ν is a threshold angle, penalizes the regions of $\partial\Omega$ where the angle between the normal vector n and the negative vertical direction $-e_d$ is smaller than ν.
- The choice

$$\varphi_p(n) = \prod_{i=1}^m (n - n_{\psi_i})^2, \tag{3.3}$$

  where the $\psi_i : \mathbb{R}^d \to \mathbb{R}$, $i = 1, ..., m$ are given *pattern functions*, and $n_{\psi_i} := \frac{\nabla\psi_i}{|\nabla\psi_i|}$ are the corresponding normalized gradients, compels n to be close to at least one of the directions n_{ψ_i}.

In the sequel, we denote by $P_a(\Omega)$ and $P_p(\Omega)$ the constraint functionals arising from (3.1) in the respective cases where $\varphi \equiv \varphi_a$ and $\varphi \equiv \varphi_p$. When it comes to the shape derivatives of these functionals, the result of interest is the following [14].

Proposition 3.1. *The shape functional $P_g(\Omega)$ defined by (3.1) is shape differentiable at any admissible shape $\Omega \in \mathcal{U}_{\rm ad}$ when deformations θ are in Θ^k, $k \geq 1$. Its shape derivative reads:*

$$P_g'(\Omega)(\theta) = \int_\Gamma \kappa\, \varphi(n)\, \theta \cdot n\, ds - \int_\Gamma \nabla_{\partial\Omega}(\varphi(n)) \cdot \nabla_{\partial\Omega}(\theta \cdot n)\, ds,$$

where $\nabla_{\partial\Omega}\psi := \nabla\psi - (\nabla\psi \cdot n)n$ is the tangential gradient of a smooth enough function $\psi : \partial\Omega \to \mathbb{R}$.

Remark 3.1. *Although the normal vector n is a priori defined only on the boundary $\partial\Omega$, it can always be extended in a neighborhood of the boundary (at least when Ω is sufficiently smooth). Thus, there is no difficulty in defining the full gradient ∇n and furthermore the tangential gradient $\nabla_{\partial\Omega} n$ is independent of such an extension of n.*

Anticipating a little on the numerical discussion of Section 5 - see notably Section 5.2.3 about the *dripping effect* - such geometric functionals turn out to have serious limitations when it comes to penalizing overhang features. This calls for the device of other types of constraint functionals.

4. Presentation of the mechanical constraint functionals

As an alternative to the geometric functionals of Section 3, we now introduce mechanical constraint functionals, bringing into play the physical behavior of shapes during the construction process. To this end, we rely on the results obtained in [3], and we also elaborate on the model discussed in there.

4.1. Modeling of the construction process.

In the context of their fabrication, the shapes Ω are contained in a fixed working domain $D = S \times (0, H)$ (where $S \subset \mathbb{R}^{d-1}$) representing the build chamber.

In order to mimic the layer by layer construction of Ω, we consider the *intermediate shapes*

$$\Omega_h := \{x = (x_1, ..., x_d) \in \Omega,\ 0 < x_d < h\}, \quad h \in (0, H),$$

which roughly speaking correspond to particular snapshots taken during the construction process. We use a decomposition of $\partial\Omega_h$ which slightly differs from that in Section 2.1: $\partial\Omega_h$ now reads: $\partial\Omega_h = \Gamma_0 \cup \Gamma_h^l \cup \Gamma_h^u$, where:

- $\Gamma_0 = \{x \in \partial\Omega_h,\ x_d = 0\}$ is the contact region between Ω_h and the build table,
- $\Gamma_h^u = \{x \in \partial\Omega_h,\ x_d = h\}$ is the upper side of Ω_h,
- $\Gamma_h^l = \partial\Omega_h \setminus (\overline{\Gamma_0} \cup \overline{\Gamma_h^u})$ is the lateral surface of $\partial\Omega_h$.

We also introduce the part $\ell_h := \{x \in \partial\Omega,\ x_d = h\}$ of the boundary $\partial\Omega$ lying at height h (typically, ℓ_h is a curve in three space dimensions, which is the boundary of Γ_h^u in the plane $x_d = h$); see Figure 5 about these notations.

Remark 4.1. *Let us point out an important bias in the above model for the manufacturing process: it implicitly relies on the assumption that every layer of material is constructed instantaneously (and so, it does not see the way each such layer is assembled). This feature has important consequences on the interpretation of the numerical results; see Section 5.3.*

4.2. The self-weight manufacturing compliance $P_{\rm sw}(\Omega)$.

At an arbitrary stage $h \in (0, H)$ of the construction process, the intermediate shape Ω_h is only submitted to gravity effects, accounted for by a (smooth) body force $g : \mathbb{R}^d \to \mathbb{R}^d$. In this context, the elastic displacement of Ω_h is the unique solution $u^c_{\Omega_h} \in H^1_{\Gamma_0}(\Omega_h)^d$ to the construction system:

$$\left\{ \begin{array}{rcll} -\mathrm{div}(Ae(u^c_{\Omega_h})) & = & g & \text{in } \Omega_h, \\ u^c_{\Omega_h} & = & 0 & \text{on } \Gamma_0, \\ Ae(u^c_{\Omega_h})n & = & 0 & \text{on } \Gamma_h^l \cup \Gamma_h^u. \end{array} \right. \tag{4.1}$$

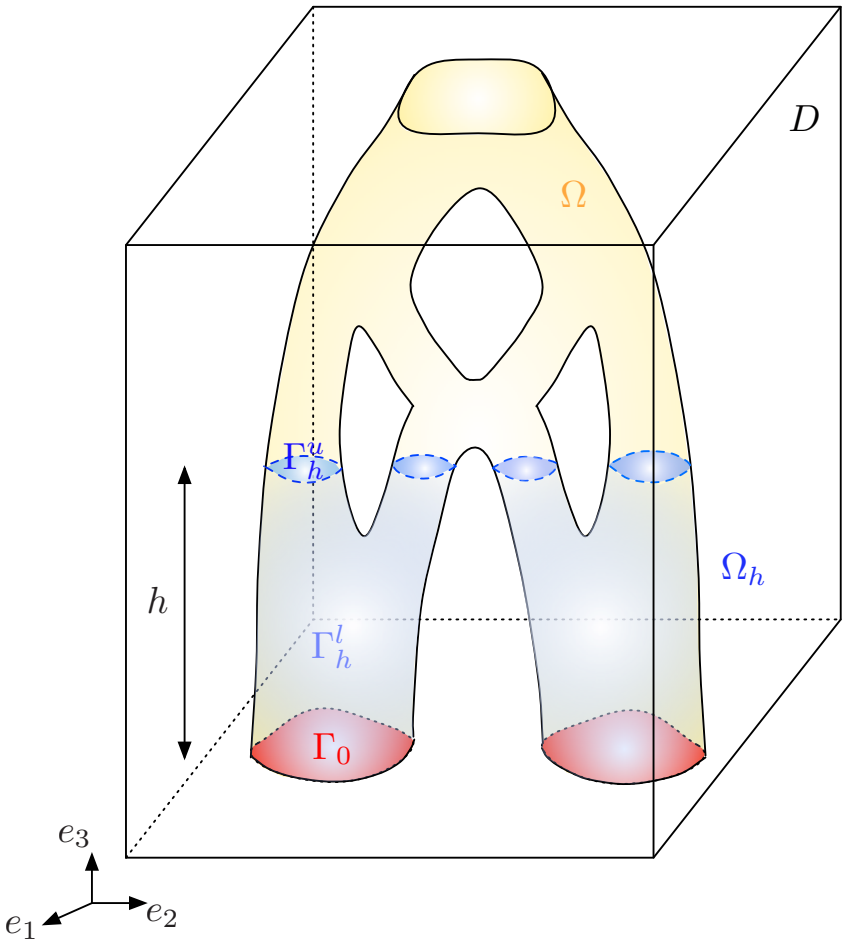

FIGURE 5. *Physical setting of the shape Ω during the additive manufacturing process.*

The *self-weight* of Ω_h then reads:

$$c_{\Omega_h} = \int_{\Omega_h} Ae(u^c_{\Omega_h}) : e(u^c_{\Omega_h})\, dx = \int_{\Omega_h} g \cdot u^c_{\Omega_h}\, dx. \tag{4.2}$$

The proposed mechanical constraint $P_{\rm sw}(\Omega)$ aggregates the self-weigths of all the intermediate structures Ω_h, $h \in (0, H)$, and therefore deserves the name of *self-weight manufacturing compliance*:

$$P_{\rm sw}(\Omega) = \int_0^H j(c_{\Omega_h})\, dh, \tag{4.3}$$

where $j : \mathbb{R} \to \mathbb{R}$ is a given smooth function.

The study of the derivative of $P_{\rm sw}(\Omega)$ with respect to the domain is not a standard issue. It has been addressed in [3], and to account for the results of interest, we need additional notations; $\Omega \in \mathcal{U}_{\rm ad}$ being a given admissible shape, we introduce:

- Two open sets $\mathcal{O}_1 \Subset \mathcal{O}_2$ in $\mathbb{R}^d$, where $\mathcal{O}_1$ is an open neighborhood of the set

$$\{x \in \partial\Omega,\ \ n(x) = \pm e_d\}$$

composed of the points on $\partial\Omega$ where the normal vector is vertical.

- A smooth cutoff function $\chi : \mathbb{R}^d \to \mathbb{R}$ such that:

$$0 \leq \chi \leq 1, \ \chi \equiv 0 \text{ on } \mathcal{O}_1, \text{ and } \chi \equiv 1 \text{ on } \mathbb{R}^d \setminus \overline{\mathcal{O}_2}.$$

- For every $k \geq 1$, the set X^k of vector fields

$$X^k := \left\{ \theta = \chi \widetilde{\theta}, \text{ where } \widetilde{\theta} \in \Theta^k \right\}.$$

In other terms, the completely flat regions of $\partial\Omega$ stay fixed under deformations $\theta \in X^k$; the motivation behind this definition is that deformations of such regions could cause some intermediate shapes to change topology, breaking the differentiability of $P_{\rm sw}(\Omega)$ with respect to Ω.

The result of interest is now the following; see [3].

Theorem 4.1. *The functional $P_{\rm sw}(\Omega)$ given by (4.3) is shape differentiable at Ω, in the sense that the mapping $\theta \mapsto P_{\rm sw}(\Omega_\theta)$, from X^k into $\mathbb{R}$ is differentiable for $k \geq 1$. Its derivative is:*

$$\forall \theta \in X^k, \ P'_{\rm sw}(\Omega)(\theta) = \int_{\partial\Omega \setminus \overline{\Gamma_0}} \mathcal{D}_\Omega \, \theta \cdot n \, ds, \tag{4.4}$$

where the integrand factor $\mathcal{D}_\Omega$ is defined for a.e. $x \in \partial\Omega \setminus \overline{\Gamma_0}$ by:

$$\mathcal{D}_\Omega(x) = \int_{x_d}^{H} j'(c_{\Omega_h}) \left(2g \cdot u^c_{\Omega_h} - Ae(u^c_{\Omega_h}) : e(u^c_{\Omega_h}) \right)(x) \, dh. \tag{4.5}$$

Remark 4.2. *Formula (4.5) for the integrand of the shape derivative $P'_{\rm sw}(\Omega)(\theta)$ has an intuitive interpretation: the sensitivity at each point $x = (x_1, ..., x_d) \in \partial\Omega$ depends on the sensitivities of the self-weights of all the intermediate structures Ω_h for $h > x_d$. Indeed the point x does not belong to Ω_h for $h < x_d$.*

4.3. **Practical algorithms for the calculation of $P_{\rm sw}(\Omega)$ and its derivative.**

The constraint $P_{\rm sw}(\Omega)$ and its shape derivative $P'_{\rm sw}(\Omega)(\theta)$ (or equivalently the integrand $\mathcal{D}_\Omega$) bring into play a continuum of shapes, and so their numerical evaluation is a priori non trivial. In this section, we consider a fixed admissible shape $\Omega \in \mathcal{U}_{\rm ad}$, and we propose two numerical algorithms for the calculation of $P_{\rm sw}(\Omega)$ and $\mathcal{D}_\Omega$.

4.3.1. *The $0^{\rm th}$-order method.*

The intuitive way to perform the aforementioned evaluations consists in discretizing the height interval $(0, H)$ into N small subintervals

$$I_i = (h_i, h_{i+1}), \ i = 0, ..., N-1, \text{ where } 0 = h_0 < h_1 < ... < h_{N-1} < h_N = H, \tag{4.6}$$

then in approximating the mappings $h \mapsto c_{\Omega_h}$ and $h \mapsto u^c_{\Omega_h}$ by constant quantities on each subinterval I_i. More precisely, our $0^{\rm th}$-order procedure for the evaluation of $P_{\rm sw}(\Omega)$ and $\mathcal{D}_\Omega$ reads:

(1) For $i = 1, ..., N$, calculate the displacements $u^c_{\Omega_{h_i}}$ by solving (4.1) and the self-weights $c_{\Omega_{h_i}}$ via (4.2).

(2) The self-weight $h \mapsto c_{\Omega_h}$ is approximated by the quantity $h \mapsto c^0(h)$ defined by:

$$c^0(h) = c_{\Omega_{h_{i+1}}} \text{ for } h \in (h_i, h_{i+1}), \ i = 0, ..., N-1.$$

(3) The displacement $h \mapsto u^c_{\Omega_h}$ is approximated by the mapping $h \mapsto u^0(h)$ given by:

$$u^0(h)(x) = u^c_{\Omega_{h_{i+1}}}(x) \text{ for } h \in (h_i, h_{i+1}) \text{ and } x \in \Omega_h, \ i = 0, ..., N.$$

Note that this makes sense since $u^c_{\Omega_{h_{i+1}}}$ is defined on $\Omega_{h_{i+1}}$, thus on Ω_h for $h \in (h_i, h_{i+1})$.

(4) $P_{\rm sw}(\Omega)$ and $\mathcal{D}_\Omega$ are approximated by the quantities P^0_N and $\mathcal{D}^0_N$ obtained by replacing c_{Ω_h} and $u^c_{\Omega_h}$ by their $0^{\rm th}$-order approximations $c^0(h)$ and $u^0(h)$ in the definitions (4.3) and (4.5) respectively.

Unfortunately, this algorithm is quite costly since the discretization (4.6) of $(0, H)$ has to be fine enough so that the accuracy of the piecewise constant approximations $c^0(h)$ and $u^0(h)$ is guaranteed.

In order to accelerate these calculations, we therefore propose a first-order interpolation method for the mappings $h \mapsto c_{\Omega_h}$ and $h \mapsto u^c_{\Omega_h}$, based on the calculation of their derivatives. Before defining this first-order method, we first introduce the required derivatives.

4.3.2. *Derivatives of the mappings $h \mapsto c_{\Omega_h}$ and $h \mapsto u^c_{\Omega_h}$.*

In this section, we consider a fixed level $h \in (0, H)$ satisfying the assumption:

$$\text{For all } x \in \ell_h, \text{ the normal vector } n(x) \text{ is different from } \pm e_d. \tag{4.7}$$

Our first result concerns the derivative of $h \mapsto c_{\Omega_h}$; see [3] for the proof.

Proposition 4.1. *The self-weight $h \mapsto c_{\Omega_h}$ is differentiable at any level h satisfying (4.7) and:*

$$\left.\frac{d}{dh}(c_{\Omega_h})\right|_h = \int_{\Gamma^u_h} \left(2g \cdot u^c_{\Omega_h} - Ae(u^c_{\Omega_h}) : e(u^c_{\Omega_h})\right) ds. \tag{4.8}$$

Giving a proper meaning to the derivative of $h \mapsto u^c_{\Omega_h}$ is a little more involved since the $u^c_{\Omega_h}$ are functions, defined on the different shapes Ω_h. This operation can nevertheless be carried out in the language of shape derivatives: roughly speaking, for small $t > 0$, the shape Ω_{h-t} may be understood as a variation of Ω_h, in an adapted sense from the definition (2.6); see Figure 6. More precisely, the following facts are proven in [3] (see also [33]).

- There exists $t_0 > 0$ and a mapping $(-t_0, t_0) \ni t \mapsto T_t$ satisfying the following properties:

  (i) For $t \in (-t_0, t_0)$, T_t is a diffeomorphism of $\mathbb{R}^d$, mapping Ω_h onto Ω_{h-t} such that:

$$T_t(\Gamma_0) = \Gamma_0, \ T_t(\Gamma^u_h) = \Gamma^u_{h-t}, \text{ and } T_t(\Gamma^l_h) = \Gamma^l_{h-t}, \tag{4.9}$$

  (ii) The mapping $t \mapsto (T_t - \mathrm{Id})$, from $(-t_0, t_0)$ into $W^{1,\infty}(\mathbb{R}^d, \mathbb{R}^d)$ is of class $\mathcal{C}^1$,

- For any mapping $t \mapsto T_t$ satisfying (4.9), introducing $V(x) := \frac{dT_t(x)}{dt}|_{t=0} \in W^{1,\infty}(\mathbb{R}^d, \mathbb{R}^d)$, one has,

$$\text{for } x \in \Gamma^u_h, \ V(x) \cdot e_d = -1, \text{ and for } x \in \Gamma^l_h, \ V(x) \cdot n(x) = 0.$$

- The mapping $t \mapsto u^c_{\Omega_{h-t}} \circ T_t$ is differentiable from $(-t_0, t_0)$ into $H^1_{\Gamma_0}(\Omega_h)^d$. Its derivative at $t = 0$ is called the *Lagrangian derivative* Y_{Ω_h} of $h \mapsto u^c_{\Omega_h}$. In general, Y_{Ω_h} depends on the mapping T_t used in its definition.
- The quantity $U_{\Omega_h} := Y_{\Omega_h} - \nabla u^c_{\Omega_h} V$ is then identified as the *Eulerian derivative* of $h \mapsto u^c_{\Omega_h}$ and is the solution in $H^1_{\Gamma_0}(\Omega_h)^d$ to the system:

$$\begin{cases} -\mathrm{div}(Ae(U_{\Omega_h})) = 0 & \text{in } \Omega_h, \\ U_{\Omega_h} = 0 & \text{on } \Gamma_0, \\ Ae(U_{\Omega_h})n = 0 & \text{on } \Gamma^l_h, \\ Ae(U_{\Omega_h})n = \frac{\partial}{\partial n}\left((Ae(u_{\Omega^c_h})n\right) & \text{on } \Gamma^u_h. \end{cases} \tag{4.10}$$

  In particular, U_{Ω_h} is independent of the mapping T_t as long as it fulfills (4.9).

In other words, the diffeomorphism T_t maps Ω_h onto Ω_{h-t} by moving only its upper boundary, leaving the other lateral and bottom boundaries fixed.

Remark 4.3. *There is a small abuse of language in referring to U_{Ω_h} as the 'Eulerian derivative' of $h \mapsto u^c_{\Omega_h}$. Strictly speaking, U_{Ω_h} is the 'right derivative' of the mapping $t \mapsto u_{\Omega_{h-t}}$ as $t \to 0^+$, and not that of $t \mapsto u_{\Omega_{h+t}}$ as t goes to zero with positive or negative values. This choice is motivated by the fact that, for a fixed level h and small $t > 0$, it naturally gives rise to a first-order Taylor formula for $u_{\Omega_{h-t}}$ which makes sense as a function on the domain Ω_{h-t} (see formula (4.12) below).*

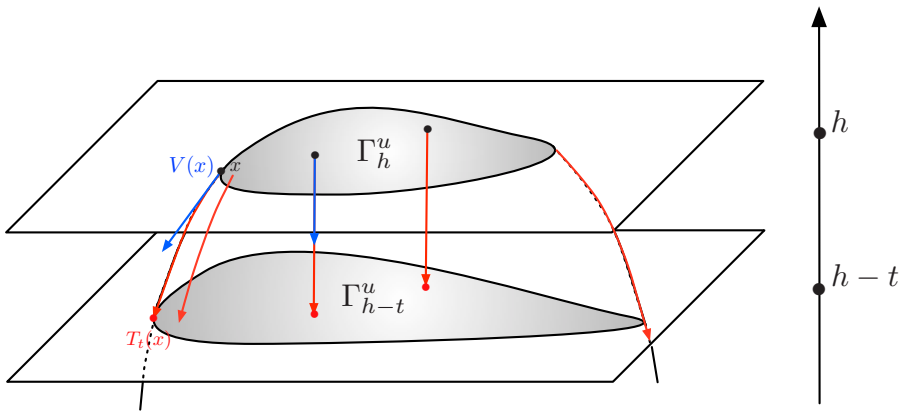

FIGURE 6. *Example of one diffeomorphism T_t of $\mathbb{R}^d$ mapping Ω_h onto Ω_{h-t}, satisfying (4.9).*

4.3.3. *The 1st-order method.*

Relying again on a discretization (4.6) of the interval $(0, H)$, our first-order procedure for approximating $P_{\rm sw}(\Omega)$ and $\mathcal{D}_\Omega$ unfolds as follows:

(1) For $i = 0, ..., N$, calculate the displacements $u^c_{\Omega_{h_i}}$ by solving (4.1) and the self-weights $c_{\Omega_{h_i}}$ according to (4.2) (for $i = 0$, these quantities vanish).
(2) For $i = 0, ..., N$, compute the derivative $\frac{d}{dh}(c_{\Omega_h})\big|_{h=h_i}$ with Proposition 4.1 (for $i = 0$, it is zero).
(3) For $i = 1, ..., N$, calculate the Eulerian derivative $U_{\Omega_{h_i}}$ at h_i by using (4.10).
(4) The first-order reconstruction $c^1(h)$ of $h \mapsto c_{\Omega_h}$ coincides on each interval $I_i = (h_i, h_{i+1})$ with the cubic spline $h \mapsto c^1_i(h)$ which is uniquely determined by the data:

$$c^1_i(h_i) = c_{\Omega_{h_i}},\ c^1_i(h_{i+1}) = c_{\Omega_{h_{i+1}}},\ c^{1\prime}_i(h_i) = \frac{d}{dh}(c_{\Omega_h})\Big|_{h_i},\ \text{and } c^{1\prime}_i(h_{i+1}) = \frac{d}{dh}(c_{\Omega_h})\Big|_{h_{i+1}}. \tag{4.11}$$

(5) The first-order reconstruction $u^1(h)$ of $h \mapsto u^c_{\Omega_h}$ is given for $h \in I_i$ by:

$$u^1(h)(x) = u^c_{\Omega_{h_{i+1}}}(x) + (h_{i+1} - h)\, U_{\Omega_{h_{i+1}}}(x) \text{ for } x \in \Omega_h. \tag{4.12}$$

Again, (4.12) makes sense for $x \in \Omega_h$, $h \in (h_i, h_{i+1})$ since $u^c_{\Omega_{h_{i+1}}}$ and $U_{\Omega_{h_{i+1}}}$ are both well-defined on $\Omega_h \subset \Omega_{h_{i+1}}$. Note that $u^1(h)$ is not continuous with respect to h.
(6) $P_{\rm sw}(\Omega)$ and $\mathcal{D}_\Omega$ are approximated by the quantities P^1_N and $\mathcal{D}^1_N$ obtained by replacing c_{Ω_h} and $u^c_{\Omega_h}$ by their 1st-order approximations $c^1(h)$ and $u^1(h)$ in (4.3) and (4.5) respectively.

4.4. **Alternative mechanical models of the behavior of intermediate shapes.**

Our device of the constraint $P_{\rm sw}(\Omega)$ in Section 4.2 is guided by the description (4.1) of the physical behavior of the intermediate shapes Ω_h in the course of the construction process: they are only subjected to gravity effects.

However, different mechanical models could be considered instead of (4.1), including fictitious ones, thereby giving different focuses to the constraint functional. In this spirit, we propose in this section an alternative construction to that of Section 4.2 which brings into play an artificial force, applied on the upper region of each intermediate shape Ω_h. More precisely, each intermediate shape Ω_h is now subjected to a body force $g_h \in L^2(\mathbb{R}^d)^d$ defined by:

$$g_h(x) = \begin{cases} g & \text{if } x_d \in (h - \delta, h), \\ 0 & \text{otherwise,} \end{cases} \tag{4.13}$$

where $\delta > 0$ is a small parameter, and $g \in L^2(\mathbb{R}^d)^d$ is a given function. The elastic displacement $u^a_{\Omega_h}$ of Ω_h in this context is the unique solution in $H^1_{\Gamma_0}(\Omega_h)^d$ to the system:

$$\left\{ \begin{array}{cc} -\mathrm{div}(Ae(u^a_{\Omega_h})) = g_h & \text{in } \Omega_h, \\ u^a_{\Omega_h} = 0 & \text{on } \Gamma_0, \\ Ae(u^a_{\Omega_h})n = 0 & \text{on } \Gamma^l_h \cup \Gamma^u_h. \end{array} \right. \tag{4.14}$$

The related *upper-weight* of Ω_h then reads:

$$c^a_{\Omega_h} = \int_{\Omega_h} Ae(u^a_{\Omega_h}) : e(u^a_{\Omega_h})\, dx = \int_{\Gamma^u_h} g \cdot u^a_{\Omega_h}\, ds,$$

and the corresponding *upper-weight manufacturing compliance* reads:

$$P_{\mathrm{uw}}(\Omega) = \int_0^H j(c^a_{\Omega_h})\, dh. \tag{4.15}$$

As we shall see in Section 5, this formulation is well-suited when it comes to penalizing more specifically the upper region of each intermediate shape Ω_h.

As far as the shape derivative of $P_{\mathrm{uw}}(\Omega)$ is concerned, the exact same proof as in [3] can be worked out (taking advantage of the definition (4.13) of g_h), and the conclusions of Theorem 4.1 extend verbatim to this new case. Also, using a similar analysis to that of Section 4.3 (and working out similar calculations as in [3]), it is possible to calculate the 'derivatives' of the mappings $h \mapsto c^a_{\Omega_h}$ and $h \mapsto u^a_{\Omega_h}$, which look very much like the expressions (4.8) and (4.10), up to additional terms accounting for the dependence of the load g_h on h.

Let us eventually emphasize that our choice of the linearized elasticity systems (4.1) or (4.14) for the description of the behavior of the intermediate shapes is merely incidental. One could for instance rely on a similar construction, involving instead the heat equation, so as to model cooling effects within the intermediate shapes, and thereby residual stresses; see [4] about this idea.

5. Numerical examples

In this section, we conduct several numerical experiments to put the constraint functionals introduced in this work to the test.

5.1. **Description of the numerical framework.**

Let us first and foremost provide some technical details about the practical implementation of the examples discussed hereafter.

When it comes to the numerical representation of shapes and their deformations, the level set method on a fixed computational mesh is used because of its robustness and versatility; see [34, 35, 40] for general considerations about the level set method, and [5, 41, 43] about its use in the shape optimization context. In a nutshell, one shape Ω, enclosed in a larger, fixed working domain D is regarded as the negative subdomain of a scalar 'level set' function $\phi : D \to \mathbb{R}$, that is:

$$\left\{ \begin{array}{ll} \phi(x) < 0 & \text{if } x \in \Omega, \\ \phi(x) = 0 & \text{if } x \in \partial\Omega, \\ \phi(x) > 0 & \text{if } x \in D \setminus \overline{\Omega}. \end{array} \right. \tag{5.1}$$

The evolution in time of a shape $\Omega(t)$, driven by a velocity field with normal component $V(t,x)$, can be modeled by the following Hamilton-Jacobi equation, the solution $\phi(t,x)$ of which, is a level set function for $\Omega(t)$:

$$\frac{\partial \phi}{\partial t}(t,x) + V(t,x)|\nabla \phi(t,x)| = 0, \;\; t > 0, \;\; x \in D. \tag{5.2}$$

In our applications, the (scalar) velocity field $V(t,x)$ stems from the resolution of Problem (2.4) or (2.5) by means of an SLP-type optimization algorithm similar to those presented in [17, 45], based on the derivatives of $J(\Omega)$ and $P(\Omega)$.

From a numerical point of view, the working domain D is a box in two or three space dimensions; it is discretized by means of a Cartesian mesh $\mathcal{G}$, i.e. $\mathcal{G}$ is composed of square elements in $2d$ and cubes in $3d$. The level set function ϕ is discretized at the vertices of $\mathcal{G}$ and the Hamilton-Jacobi equation (5.2) is solved by using an explicit second-order upwind scheme on $\mathcal{G}$, as presented e.g. in [34, 40].

Since the computational mesh $\mathcal{G}$ is fixed throughout the optimization process of the shape Ω, no mesh of Ω is available for the Finite Element resolution of linearized elasticity systems of the form (2.1). To circumvent this difficulty, we rely on the so-called 'ersatz-material' approximation which consists in filling the void $D\setminus\overline{\Omega}$ with a very soft material with Hooke's tensor εA (in practice $\varepsilon = 10^{-3}$), thus transferring a system posed on Ω into an approximate one posed on D; see for instance [5].

We rely on $\mathbb{Q}_1$ Lagrange Finite Elements coded in `Scilab` [11] for all the two-dimensional computations performed in this article, except for the tests regarding the first-order algorithm in Sections 5.3.1 and 5.3.2. For the latter calculations, as well as for the three-dimensional Finite Element resolutions, we use the `FreeFem++` environment [21]: Lagrange $\mathbb{P}_1$ elements are used on a simplicial mesh of D, obtained by splitting each square element of $\mathcal{G}$ into two triangles in 2d, and each cubic element of $\mathcal{G}$ into six tetrahedra in 3d [18].

In all the examples, the Young's modulus of the considered elastic material is normalized as $E = 1$ and the Poisson's ratio is set to $\nu = 0.33$.

When it comes to our numerical experiments about the mechanical constraints of Section 4, the integrand function featured in the definitions (4.3) and (4.15) is $j(s) = s$. Except in the examples of Section 5.3.1 and 5.3.2, where it is explicitly specified, we rely on the 0^{th}-order algorithm for the evaluation of the constraint functionals and their derivative, using a uniform subdivision $\{h_i\}_{i=0,\dots,N}$ of the height interval $(0, H)$. Indeed, the results produced by the first-order procedure in $3d$ situations, or when using the upper-weight manufacturing compliance constraint $P_{\text{uw}}(\Omega)$, are not so convincing as those of Sections 5.3.1 and 5.3.2. We believe that this is mainly caused by our numerical environment, which does not allow us to use a finer space discretization, as would be required to carry out accurate enough computations.

Let us finally emphasize that no particular programming effort has been devoted to making our implementation computationnally efficient. For instance, all the Finite Element resolutions of (4.1) or (4.14), which are needed for the evaluation of the mechanical constraints and their derivative, associated to the intermediate shapes Ω_h of a single shape Ω could trivially be performed in parallel, which is not the case in this work. Also, the communication between the optimization algorithm and the Finite Element solver is achieved via file exchange, which is a notorious source of inefficiency.

5.2. **Evaluation of the efficiency of the geometric functionals.**

Our first set of numerical experiments is devoted to the geometric constraint functionals of Section 3.

5.2.1. *Two-dimensional cantilever beam.*

In this example, we consider a two-dimensional cantilever beam, enclosed in a working domain D with size 0.5×1. In the context of its final utilization, the structure is clamped at its lower boundary and a horizontal load $f = (1, 0)$ is applied at the middle of its upper side (see Figure 7). When it comes to its construction, the shape is built from bottom to top, so that Γ_0 coincides with Γ_D. The domain D is meshed with 100×200 $\mathbb{Q}_1$ elements.

Starting from the initial shape Ω^0 of Figure 8 (a), we first minimize the structural compliance of shapes under a volume constraint, i.e. we solve:

$$\begin{array}{ll} \min\limits_{\Omega} & J(\Omega) \\ \text{s.t.} & \text{Vol}(\Omega) \leq \alpha_v \text{Vol}(D) \end{array} \tag{5.3}$$

with the value $\alpha_v = 0.2$. The resulting optimized design Ω^* is represented on Figure 8 (b). Notice that Ω^* presents two overhanging bars, i.e. forming a small angle with the horizontal direction.

In order to penalize the emergence of such features, starting from the same initial shape, we solve, instead of (5.3), the new optimization problem:

$$\begin{array}{ll} \min\limits_{\Omega} & (1-\alpha_g)\frac{J(\Omega)}{J(\Omega^*)} + \alpha_g \frac{P_g(\Omega)}{P_g(\Omega^*)} \\ \text{s.t.} & \text{Vol}(\Omega) \leq \alpha_v \text{Vol}(D) \end{array}, \tag{5.4}$$

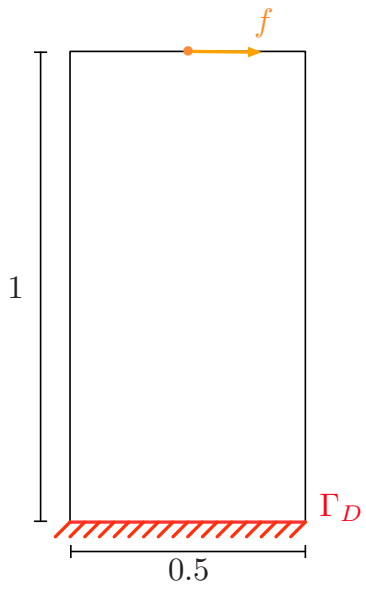

FIGURE 7. *Setting of the two-dimensional cantilever beam test case.*

for different values of the weight $\alpha_g \in [0,1]$, where the constraint $P_g(\Omega)$ defined by (3.1) is cooked from one of the functions φ_a or φ_p defined in (3.2) and (3.3).

We first use the integrand function $\varphi \equiv \varphi_a$ with the threshold angle $\nu = 45°$ and the parameter $\alpha_g = 0.01$; the resulting optimized structure is represented on Figure 8 (c). The overhanging regions have been reduced thanks to the addition of intermediate bars, but they have not totally disappeared.

Let us now consider the choice $\varphi \equiv \varphi_p$ as in (3.3), with the pattern functions $\psi_i : \mathbb{R}^2 \to \mathbb{R}$ defined by:

$$\psi_i(x) := n_{\psi_i} \cdot x, \text{ where } n_{\psi_i} = (\cos\nu_i, \sin\nu_i) \text{ and } \nu_i = -\frac{\pi}{4} + \frac{6i\pi}{40}, \ \ i = 0, ..., 10; \tag{5.5}$$

in other terms, the corresponding constraint functional $P_p(\Omega)$ imposes the orientation of the boundary $\partial\Omega$ to comply with that of one of the straight lines with normal vector n_{ψ_i}. These directions n_{ψ_i} are uniformly sampled among the set of those making an angle with the negative vertical direction comprised in $[\frac{\pi}{4}, \frac{5\pi}{4}]$. The resulting optimal shape is depicted on Figure 8 (d), and it is free of overhangs.

The values of the structural compliance, volume and constraint functionals in the above cases are reported in Table 1. Interestingly, the optimized shape in Figure 8 (d) is better than that in Figure 8 (c) with respect to both functionals $P_a(\Omega)$ and $P_p(\Omega)$ (and also in terms of the structural compliance $J(\Omega)$). This suggests that the optimization process for Problem (5.4) has fallen into a (bad) local minimum in the case where the geometric functional $P_a(\Omega)$ was used. This trend showed up in many of our numerical experiments about the used of the geometric functionals $P_a(\Omega)$ and $P_p(\Omega)$; it suggests that $P_a(\Omega)$ has 'more' local minima than $P_p(\Omega)$, and so we believe that the use of the former is awkward in the shape optimization context.

Optimization problem	$J(\Omega)$	$\mathrm{Vol}(\Omega)$	$P_a(\Omega)$	$P_p(\Omega)$
Problem (5.3)	141.25	0.400	0.032	12091
Problem (5.4) using $P_a(\Omega)$	151.05	0.400	0.028	13812
Problem (5.4) using $P_p(\Omega)$	147.37	0.400	0.004	3338

TABLE 1. *Values of the compliance, the volume and the geometric constraints $P_a(\Omega)$ and $P_p(\Omega)$ for the optimized designs obtained in the 2d cantilever example of Section 5.2.1.*

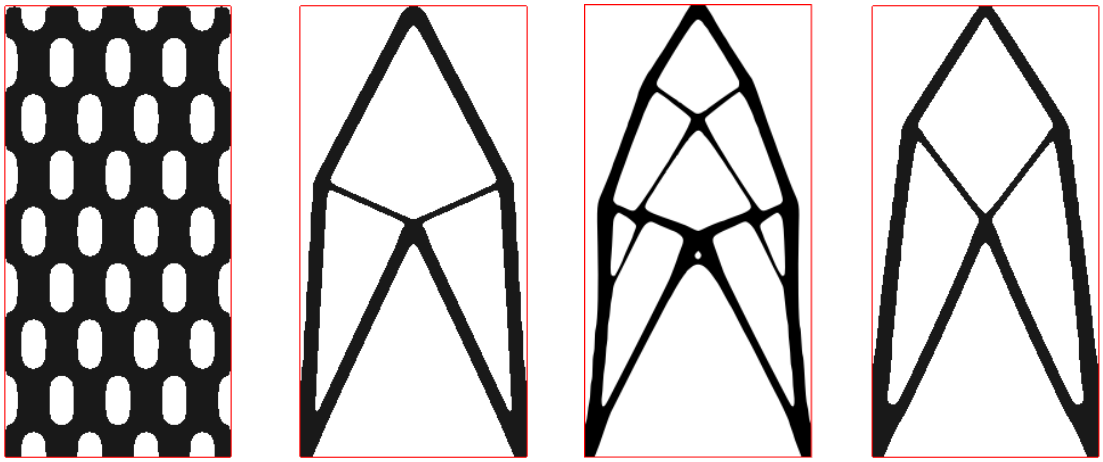

FIGURE 8. *Penalization of the overhang features in the 2d cantilever of Section 5.2.1 using geometric constraints: (a) initial shape Ω^0, (b) optimized shape Ω^* for Problem (5.3), (c) optimized shape for Problem (5.4) using $\varphi = \varphi_a$, $\nu = 45°$, and $\alpha_g = 0.01$, (d) optimized shape using $\varphi = \varphi_p$, $\alpha_g = 0.02$ and the patterns defined by (5.5).*

Remark 5.1. *Let us already point out an important limitation in the ability of the geometric functionals $P_a(\Omega)$ and $P_p(\Omega)$ to penalize the presence of overhang features. Obviously, the negative vertical direction $-e_d$ is the local maximizer of the integrands $\varphi_a(n)$ and $\varphi_p(n)$ defined by (3.2) and (3.3) (at least with the choice (5.5) for the patterin functions ψ_i), and so the shape gradients of $P_a(\Omega)$ and $P_p(\Omega)$ equal 0 in the completely horizontal regions of Ω (see Proposition 3.1). In particular, removing the possible nearly horizontal overhanging features on the initial shape Ω_0 is likely to fail with such strategies - a difficulty we experienced in using the shape Ω^* displayed on Figure 8 (b) as initial shape for the optimization problem (5.4).*

5.2.2. *Two-dimensional MBB beam.*

Our second example is the benchmark two-dimensional MBB Beam of size 6×1, as depicted in Figure 9. The structure is anchored at its bottom-right corner, and the vertical displacement is set to 0 at its bottom-left corner. A unit vertical load $f = (0, -1)$ is applied at the middle of its upper side. Here again, from the manufacturing point of view, the shape is assembled from bottom to top, i.e. Γ_0 coincides with the lower side of D. Taking advantage of the symmetry of the mechanical problem, only half the working domain D is considered during the optimization process; it is meshed by using 300×100 $\mathbb{Q}_1$ elements.

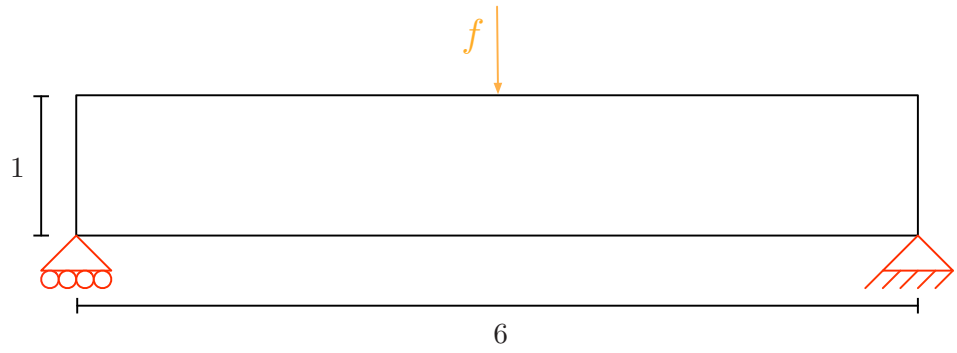

FIGURE 9. *Setting of the two-dimensional MBB beam example.*

Starting from the initial shape of Figure 10 (top), we solve the compliance minimization problem (5.3) with the threshold $\alpha_v = 0.3$ for the volume constraint. The optimized design Ω^* is represented in Figure 10 (bottom) and contains large overhanging regions. Contrary to the previous example, the overhangs in this situation are of great physical significance for the performance of Ω^*; hence, it is expected that their removal will prove more difficult than in the context of Section 5.2.1.

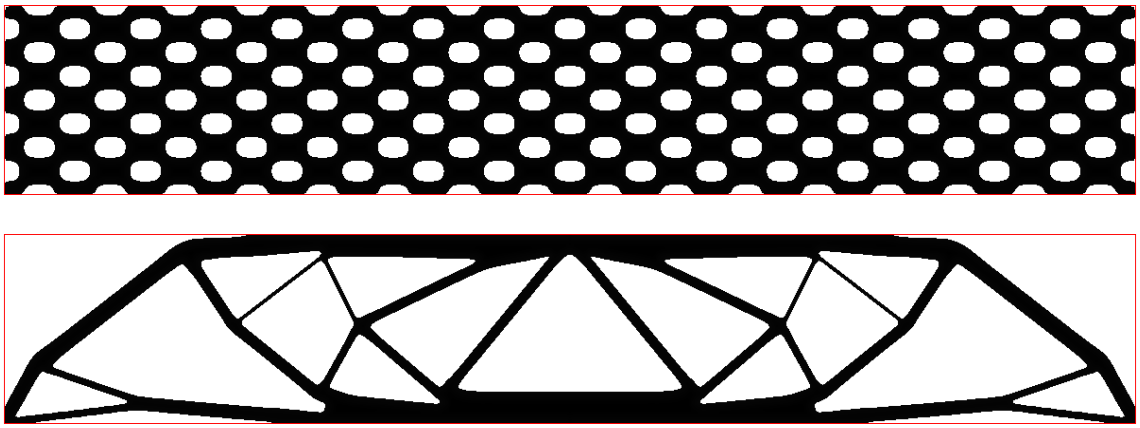

FIGURE 10. *(Top) initial and (bottom) optimized shapes for Problem (5.3) in the two-dimensional MBB Beam test-case of Section 5.2.2.*

The results displayed in Figure 11 are typical of the 'optimized' shapes resulting from the use of geometric functionals such as $P_a(\Omega)$ or $P_p(\Omega)$ to penalize the overhangs formed by members of such great structural significance. They are obtained by solving problem (5.4) with the parameter $\alpha_g = 0.50$, using

- the function φ_a given by (3.2) and the threshold angle $\nu = 45°$ as for Figure 11 (top),
- the function φ_p given by (3.3) and the pattern functions ψ_i defined in (5.5) as for Figure 11 (bottom).

One first observes that several parts in the resulting designs do comply with the desired orientation, but these are the parts whose structural significance is negligible.

More importantly, oscillations arose on the boundaries of some members, in particular those which are close to horizontal and bear a great part of the loading. This *dripping effect* has already been observed in the literature; see for instance [39]. The next subsection is devoted to a better understanding of its origin, which is a strong indicator of why geometric criteria based on angle violation are in general not sufficient ingredients to overcome overhang features.

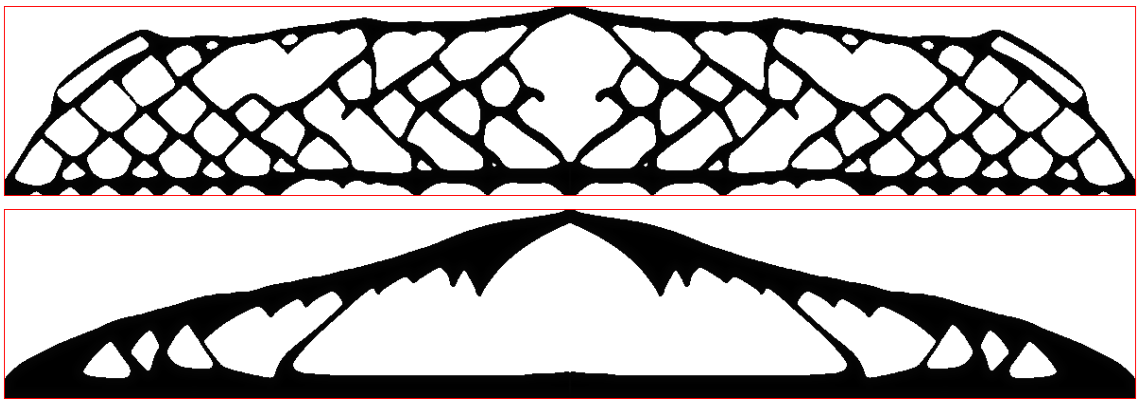

FIGURE 11. *Optimized shapes resulting from Problem (5.4) in the two-dimensional MBB Beam example, using (top) $\varphi \equiv \varphi_a$ and the threshold angle $\nu = 45°$, and (bottom) $\varphi \equiv \varphi_p$ and the pattern functions ψ_i defined in (5.5).*

5.2.3. *The 'dripping' effect.*

As we have mentioned, the 'dripping' effect is the trend for shapes to develop oscillatory boundaries within the prescribed threshold angle. From a mathematical standpoint, this effect is caused by the many local minimizers of anisotropic perimeter functionals of the form (3.1). For instance, in the optimized shapes of Figure 11, the constraint with respect to the imposed angle between the structural boundary and the horizontal directions is violated at only few points, namely at the cusps of the dripping patterns. Depending on the discretization, these points may not even be detected in the evaluation of $P_g(\Omega)$.

To better appraise this point, let us consider the following simple situation, where no mechanical objective function is involved: starting from the half-domain initial design depicted on Figure 12 (a), we minimize the angle-based functional $P_a(\Omega)$ for a threshold angle $\nu = 45^\circ$ without adding any constraint to the problem; namely, we solve:

$$\min_{\Omega} P_a(\Omega). \tag{5.6}$$

The resulting shape is represented on Figure 12 (b), and it is far from what we would have expected a priori, namely a half-space with 45° orientation with respect to the horizontal direction. The 'dripping' effect is blatant; it leads to a dramatic decrease in the value of $P_a(\Omega)$ by creating oscillations on the structural boundary, as can be observed on the convergence diagram of Figure 12 (c). Note that Figure 12 (b) even displays small inclusions of one phase (material or void) in the other one: they were created by 'pinching' flat holes, in a fashion well explained in [28] (see Figure 3.24 therein).

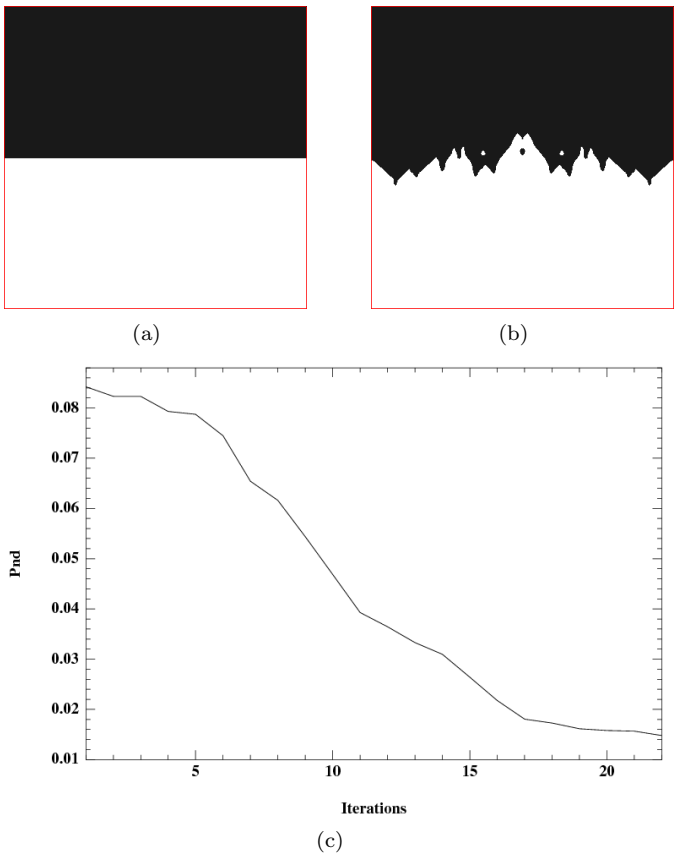

FIGURE 12. *Evaluation of the purely geometric approach and observation of the 'dripping' effect in Section 5.2.3: (a) initialization, (b) optimized shape for Problem (5.6), and (c) convergence history for the values of* $P_a(\Omega)$.

In the two-dimensional MBB Beam example of Section 5.2.2, the same effect is at play: the structure contains regions where the optimization criterion $J(\Omega)$ urges the formation of large horizontal features; the oscillatory patterns have little impact on the mechanical performance of the structure (at least when it is measured in terms of the compliance $J(\Omega)$), but they lead to a dramatic decrease in the values of the geometric functionals $P_a(\Omega)$ and $P_p(\Omega)$. Obviously, the algorithm prefers to create oscillating boundaries than rearranging the large horizontal bars, which would undermine significantly the structural performance of the shape. In this sense, the geometric criteria are not 'strong enough' to steer the algorithm to a different optimization path.

At this point, let us discuss a tempting remedy to this 'dripping' effect. An intuitive idea consists in adding a perimeter constraint to the optimization problem, with the hope that it dampens these oscillations of the boundary. To evaluate this idea, we solve a new version of Problem (5.6) which is augmented with a perimeter penalization; i.e. we solve:

$$\min_{\Omega} P_a(\Omega) + \ell \mathrm{Per}(\Omega), \tag{5.7}$$

where the coefficient ℓ is equal to 0.1.

In the same spirit, we also solve the same problem (5.4) as in Section 5.2.2, in the MBB Beam example of Figure 9, adding a perimeter penalization:

$$\begin{array}{ll} \min\limits_{\Omega} & (1-\alpha_g)\frac{J(\Omega)}{J(\Omega^*)} + \alpha_g \frac{P_g(\Omega)}{P_g(\Omega^*)} + \ell \mathrm{Per}(\Omega) \\ \text{s.t.} & \mathrm{Vol}(\Omega) \leq \alpha_v \mathrm{Vol}(D) \end{array}, \tag{5.8}$$

where $\ell = 0.1$, $\alpha_v = 0.3$ and $\alpha_g = 0.5$.

The results are displayed on Figures 13 and 14, respectively. Obviously, in both cases, the oscillations are smoothed, but the problem has not been dealt with. Admittedly, using larger values of the weight factor ℓ in (5.7) or (5.8) may make these oscillations disappear totally, but putting too much emphasis on the perimeter penalization is bound to lead to optimized designs with poor mechanical performance.

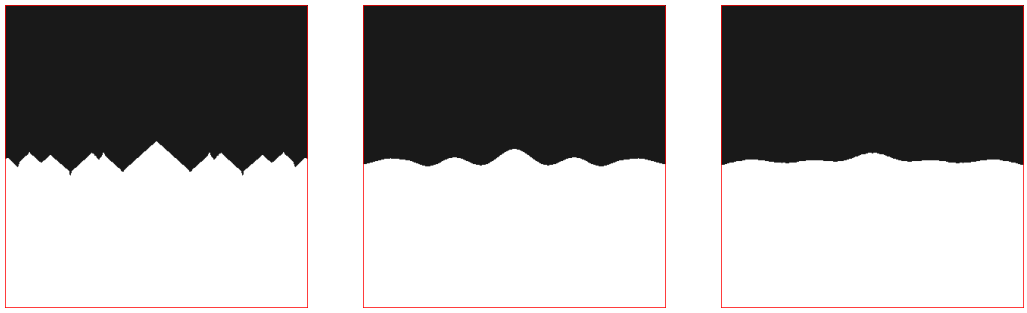

FIGURE 13. *Optimized shapes for the purely geometric Problem (5.7) under perimeter penalization, using the values (from left to right)* $\ell = 0.01$, 1 *and* 10.

FIGURE 14. *Optimized two-dimensional MBB Beam for Problem (5.8), under both a geometric and perimeter constraint.*

In a nutshell, although purely geometric approaches are computationally inexpensive, their efficiency turns out to be quite limited, even in rather simple cases.

5.3. **Evaluation of the efficiency of the mechanical functional $P_{\rm sw}(\Omega)$.**

In this section, we present numerical examples for the manufacturing compliance $P_{\rm sw}(\Omega)$ introduced in Section 4.2. We show how the incorporation of this mechanical constraint into the optimization problem leads to a different treatment of the overhanging parts and avoids the *dripping effect*. Moreover, based on the results, we test different formulations of the elasticity system describing the manufacturing context (4.1).

5.3.1. *Two-dimensional cantilever beam.*

We consider once more the two-dimensional cantilever of Section 5.2.1. The initial and optimized shapes Ω^0 and Ω^* for the compliance minimization problem under volume constraint (5.3) are the same as in Section 5.2.1 (see Figures 15 (a) and (b)).

As far as the mechanical problem simulating the manufacturing process is concerned, the physical behavior of each intermediate shape Ω_h is described by the system (4.1) where the body force g equals $(0,-1)$. We now solve the optimization problem:

$$\begin{array}{ll} \min\limits_{\Omega} & J(\Omega) \\ \text{s.t.} & \text{Vol}(\Omega) \leq \alpha_v \text{Vol}(D), \\ & P_{\rm sw}(\Omega) \leq \alpha_c P_{\rm sw}(\Omega^*). \end{array} \tag{5.9}$$

The 0^{th}-order algorithm of Section 4.3.1 is used for the evaluation of $P_{\rm sw}(\Omega)$ and its derivative, with $N = 200$ layers; in other terms, in the notation of Section 4.3.1, we calculate P^0_{200} and $\mathcal{D}^0_{200}$. In Figure 15 (c)-(e), we show the optimized shapes for (5.9) for various values of the parameter α_c, and for $\alpha_v = 0.2$. The overhanging parts disappear, and for large values of α_c, a greater amount of material is concentrated in the regions close to Γ_0; as expected, the structural compliance $J(\Omega)$ increases (yet not too dramatically) as the imposed threshold α_c becomes stricter (see Table 2).

Optimized shape	$J(\Omega)$	$\text{Vol}(\Omega)$	$P_{\rm sw}(\Omega)$
Figure 15 (b)	141.25	0.399	4226
Figure 15 (c) ($\alpha_c = 0.8$)	151.72	0.397	3365
Figure 15 (d) ($\alpha_c = 0.6$)	164.08	0.398	2528
Figure 15 (e) ($\alpha_c = 0.5$)	177.05	0.400	2106

TABLE 2. *Values of the compliance, the volume and the mechanical constraint $P_{\rm sw}(\Omega)$ for the optimized designs obtained in the 2d cantilever example of Section 5.3.1.*

Let us now evaluate the first-order algorithm of Section 4.3.3 in the present context. At first, we appraise the convergence of the approximations P^i_N and $\mathcal{D}^i_N$ for $P(\Omega)$ and $\mathcal{D}_\Omega$ respectively, in the case where Ω is the initial shape Ω^0 depicted on Figure 15 (a). To this end, we calculate the relative errors

$$\text{err}(P,N,i) = \frac{|P^i_N - P^0_{200}|}{P^0_{200}} \quad \text{and} \quad \text{err}(\mathcal{D},N,i) = \frac{||\mathcal{D}^i_N - \mathcal{D}^0_{200}||_{L^2(\partial\Omega\setminus\overline{\Gamma_0})}}{||\mathcal{D}^0_{200}||_{L^2(\partial\Omega\setminus\overline{\Gamma_0})}},$$

as functions of the size N of the subdivision. The results are reported on Figure 16.

Now, starting again from Ω^*, we solve Problem (5.9), with the parameter $\alpha_c = 0.9$, approximating $P_{\rm sw}(\Omega)$ and $\mathcal{D}_\Omega$ by the quantities P^1_{25} and $\mathcal{D}^1_{25}$. The optimized shapes are represented on Figure 17, and they are almost identical. The difference in the computational times needed to achieve them is however significant: while more than a week of calculation are needed when $P_{\rm sw}(\Omega)$ and $\mathcal{D}_\Omega$ are approximated by P^0_{200} and $\mathcal{D}^0_{200}$, less than a day is necessary when the first-order quantities P^1_{25} and $\mathcal{D}^1_{25}$ are used instead.

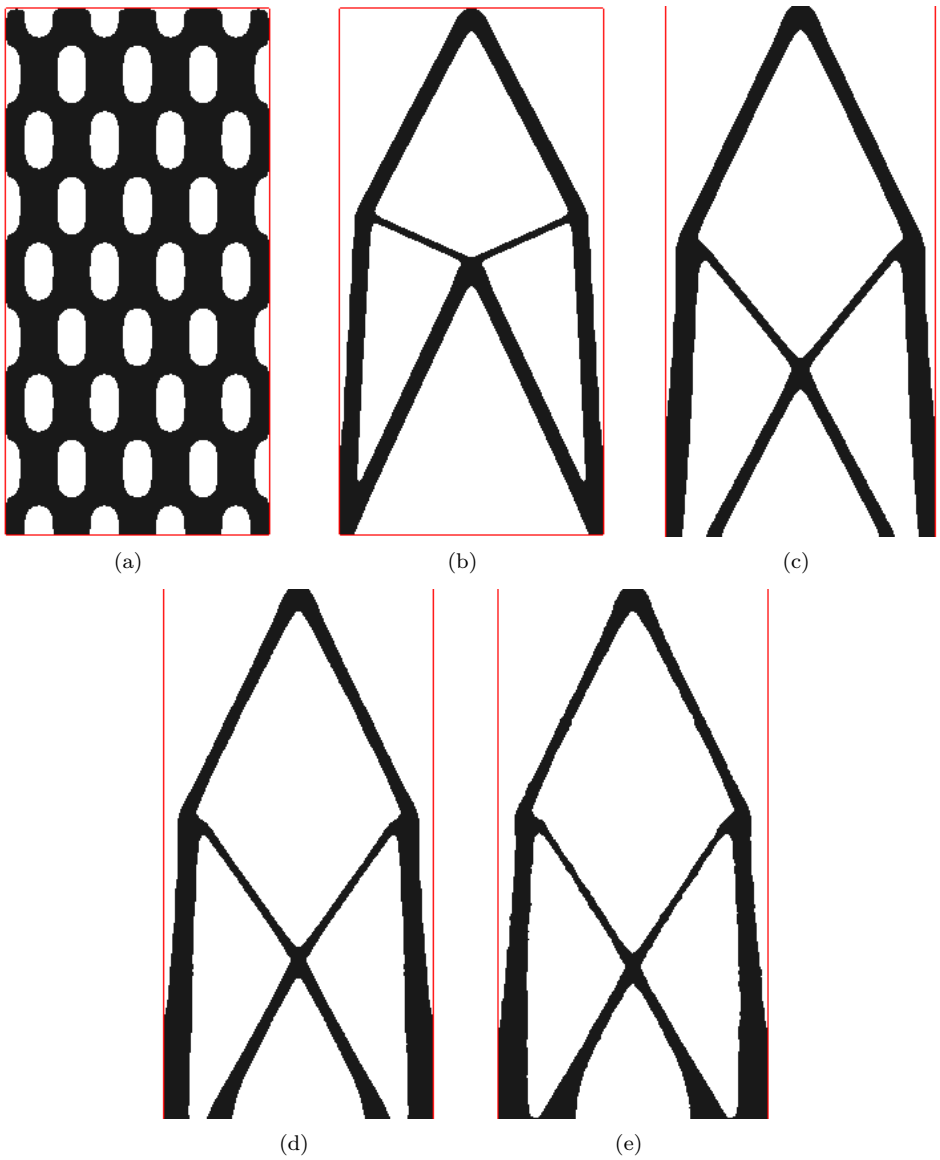

FIGURE 15. *Optimized two-dimensional cantilever beams under the self-weight manufacturing compliance constraint $P_{\mathrm{sw}}(\Omega)$, in the setting of Section 5.3.1: (a) initial shape Ω^0, (b) optimized shape Ω^* for Problem (5.3) (i.e. without additive manufacturing constraints), and optimized shapes for Problem (5.9) using the parameter (c) $\alpha_c = 0.80$; (d) $\alpha_c = 0.60$; (e) $\alpha_c = 0.50$.*

5.3.2. *Two-dimensional bridge.*

We now turn to the classical two-dimensional bridge example, as illustrated on Figure 18 (top, left): in a working domain with size 2×1, a bridge is anchored at its lower-right corner, and the vertical displacement is prevented at its lower-left corner. A vertical load $f = (0, -1)$ is applied at the middle of the lower side. The build direction of the machine tool during the construction process is oriented from the bottom to the top of the shape.

Starting from the initial shape in Figure 18 (top, right), we first solve the compliance minimization problem under volume constraint (5.3) with $\alpha_v = 0.3$, and the resulting shape Ω^* is represented on Figure

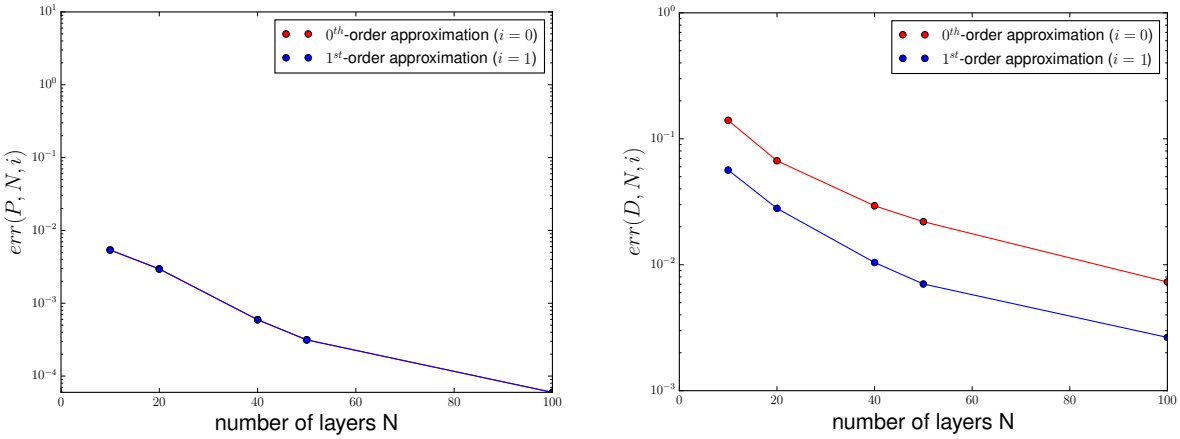

FIGURE 16. *Behavior of the errors (left)* $\mathrm{err}(P, N, i)$ *and (right)* $\mathrm{err}(\mathcal{D}, N, i)$ *as the number* N *of layers increases in the two-dimensional cantilever example of Section 5.3.1.*

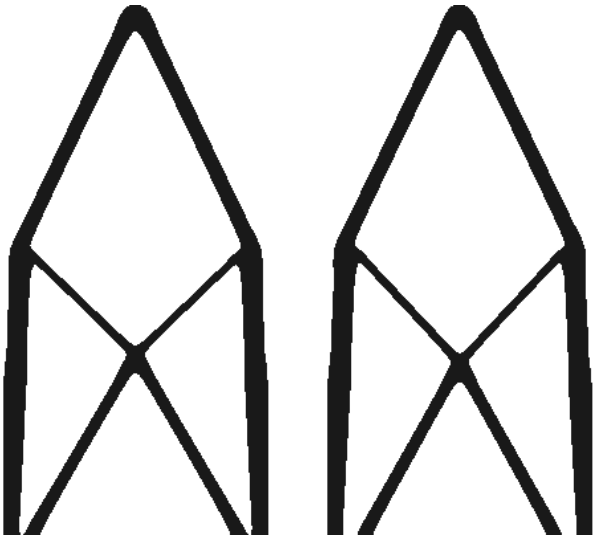

FIGURE 17. *Optimized shapes for Problem (5.9) in the two-dimensional cantilever example of Section 5.3.1, when* $P_{\mathrm{sw}}(\Omega)$ *and* $\mathcal{D}_\Omega$ *are approximated by (left)* P^0_{200} *and* $\mathcal{D}^0_{200}$*; (right)* P^1_{25} *and* $\mathcal{D}^1_{25}$*.*

18 (bottom). Notice the two overhanging bars at the bottom of Ω^*, which are consequences of the fact that the initial shape has some holes in these regions.

We then incorporate our mechanical constraint $P_{\mathrm{sw}}(\Omega)$ into the problem, i.e. we solve (5.9) with $\alpha_v = 0.3$, and for various values of α_c. To this end, we rely at first on the 0^{th}-order algorithm of Section 4.3.1 using $N = 100$ layers for the subdivision of the height interval $(0, H)$; the results are reported on Figure 20 (left column).

In a second time, we conduct the exact same experiment, using the 1^{st}-order algorithm of Section 4.3.3 for approximating $P_{\mathrm{sw}}(\Omega)$ and $\mathcal{D}_\Omega$, in combination with an *adaptive* subdivision $\{h_i\}_{i=0,\dots,N}$ of $(0, H)$, which satisfies the following rules:

(5.10)
- The maximum distance between two consecutive points h_i, h_{i+1} of the subdivision is $H/10$;
- Every value of the height h where ℓ_h contains one point where the normal vector is $\pm e_d$ (up to a tolerance) is added to the set $\{h_i\}_{i=0,\dots,N}$;

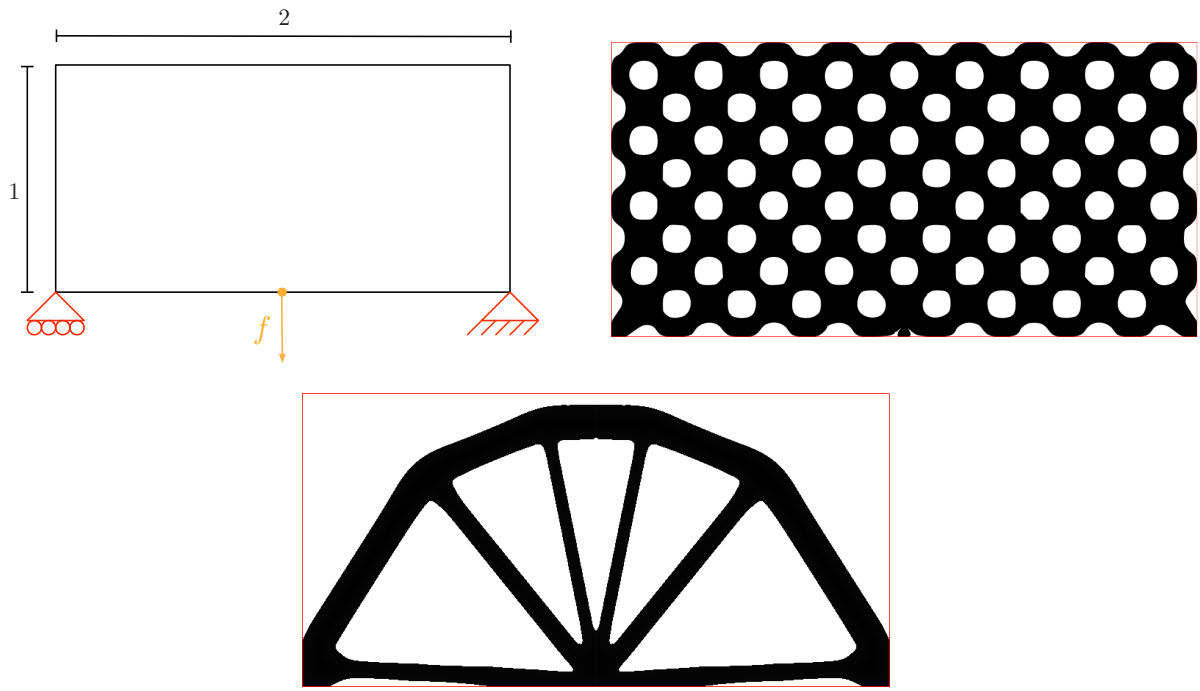

FIGURE 18. *(Top, left) setting of the two-dimensional bridge test-case, (top, right) initial shape and (bottom) optimized shape Ω^* for Problem (5.3).*

see Figure 19 for an example of such a subdivision. In practice, such a subdivision is computed at each iteration of the optimization algorithm with at least one layer every time the total volume is increased by 20% and one layer each time the normal boundary is close to minus the built direction.

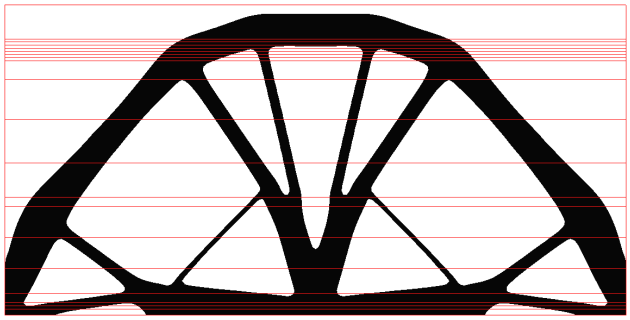

FIGURE 19. *Illustration of a subdivision of the height interval $(0, H)$ (red lines) adapted to a shape Ω (in black) according to the rules (5.10).*

The resulting optimized shapes are presented on Figure 20 (right column), and the values of the various shape functionals involved in the calculation are reported in Table 3.

Notice that the overhanging features in these optimized shapes are greatly reduced as the threshold α_c becomes stricter, but they do not completely disappear. This point is a shortcoming of the mechanical formulation of overhang constraints by means of the functional $P_{\mathrm{sw}}(\Omega)$; it will be discussed extensively in the next sections, together with possible remedies.

5.3.3. *Two-dimensional MBB beam.*

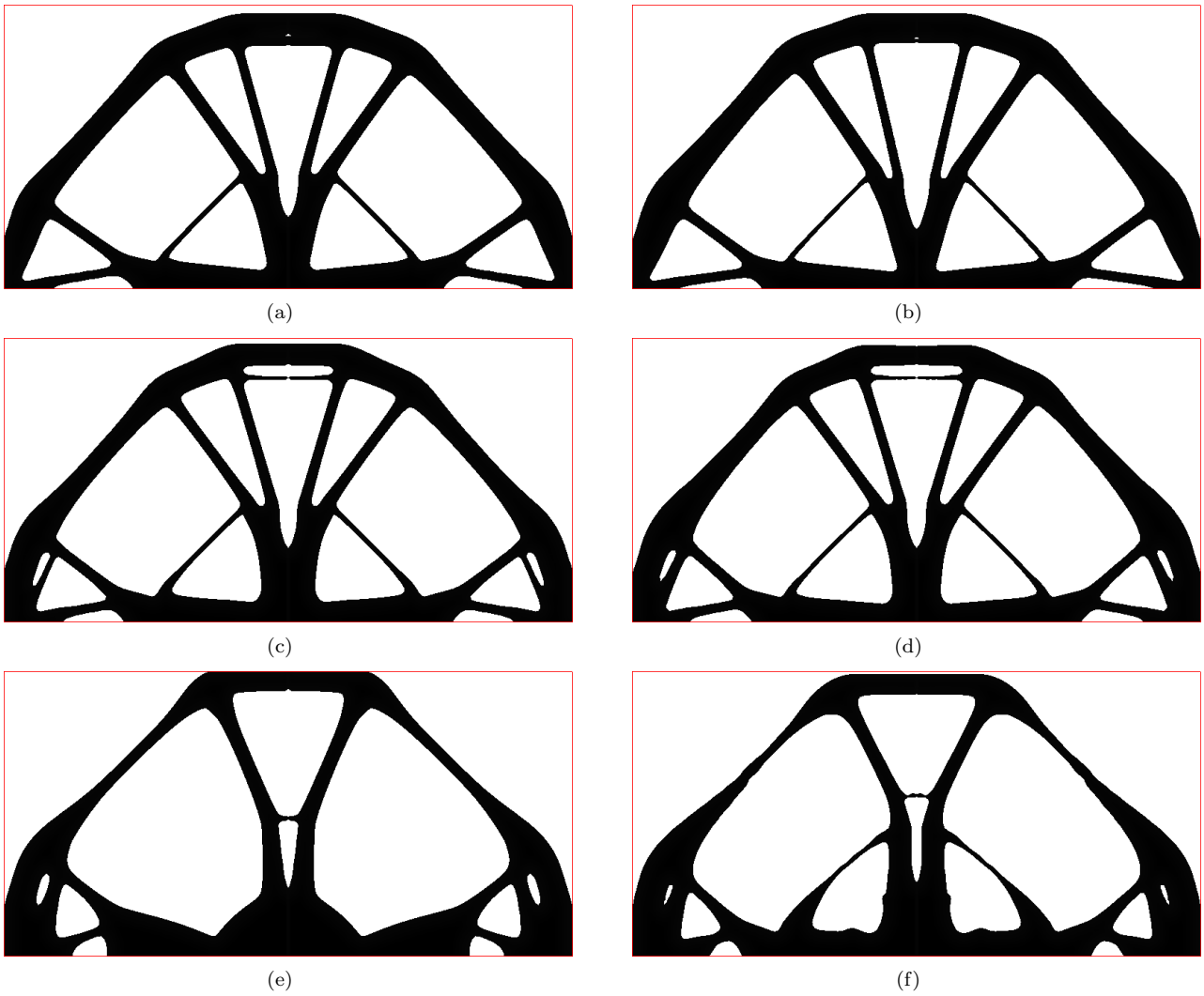

FIGURE 20. *Optimized shapes in the two-dimensional bridge test case of Section 5.3.2 (left column) no acceleration procedure is used, and (a) $\alpha_c = 0.7$, (c) $\alpha_c = 0.5$ and (e) $\alpha_c = 0.3$; (right column) the acceleration procedure is used and (b) $\alpha_c = 0.7$, (d) $\alpha_c = 0.5$ and (f) $\alpha_c = 0.3$.*

Optimized shape	$J(\Omega)$	$\mathrm{Vol}(\Omega)$	$P_{sw}(\Omega)$
Figure 18 (top, right)	43.70	0.3	5786
Figure 20 (a)	45.61	0.3	4034
Figure 20 (b)	45.29	0.3	4050
Figure 20 (c)	47.33	0.3	2810
Figure 20 (d)	47.44	0.3	2850
Figure 20 (e)	57.18	0.3	1727
Figure 20 (f)	58.77	0.3	1736

TABLE 3. *Values of the structural compliance, the volume and the manufacturing constraint $P_{sw}(\Omega)$ for the optimized designs obtained in the 2d bridge example of Section 5.3.2.*

Our third example in this section is the same two-dimensional MBB beam as that presented in Section 5.2.2; see Figure 9 for the details of the test-case. We solve the compliance minimization problem under both volume and self-weight manufacturing compliance constraints (5.9) using the 0^{th}-order algorithm of Section 4.3.1 with $N = 100$ layers, with $\alpha_v = 0.3$ and different values for the parameter α_c; the results are represented on Figure 21 (b)-(d). The values of the shape functionals involved in the optimization problem are reported in Table 4. Increasing values of α_c result in structures which are more rigid from a manufacturing point of view (i.e. with lower values of $P_{\text{sw}}(\Omega)$) and more compliant from a structural perspective (i.e. with higher values of $J(\Omega)$).

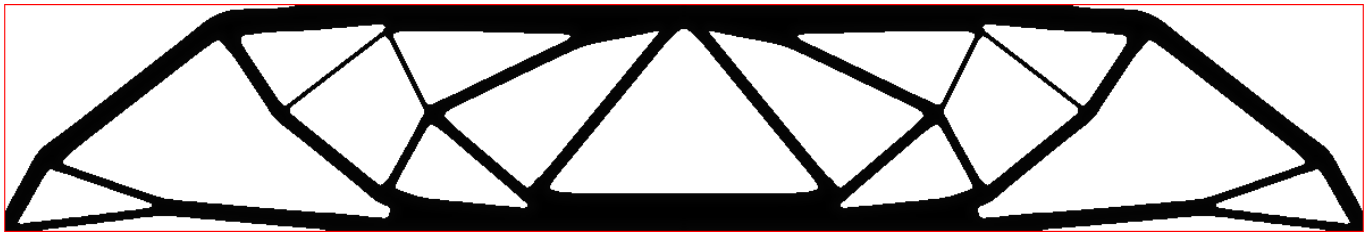

(a)

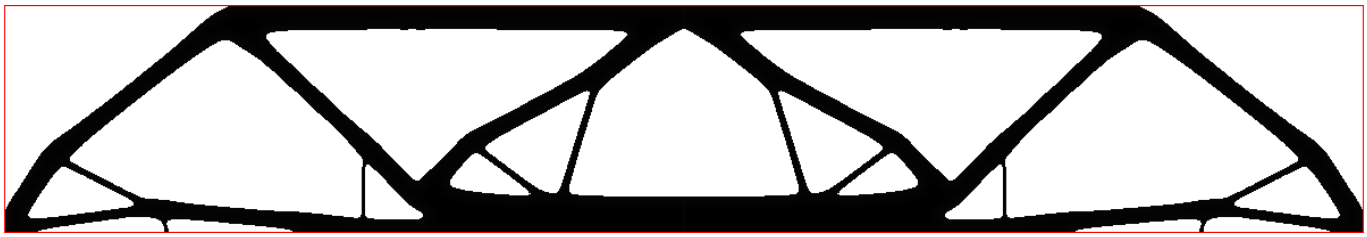

(b)

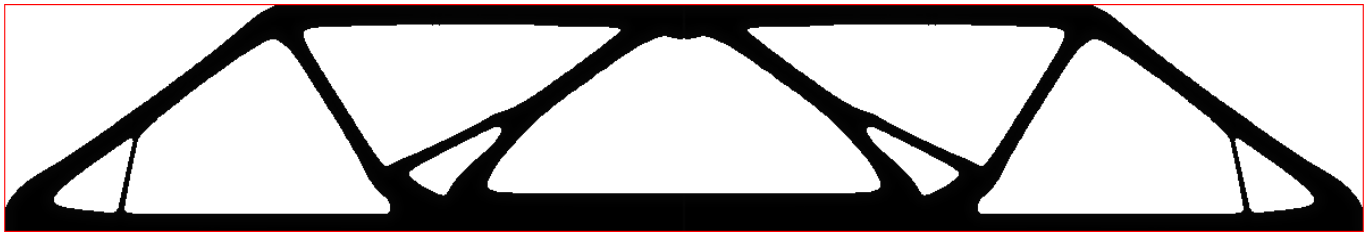

(c)

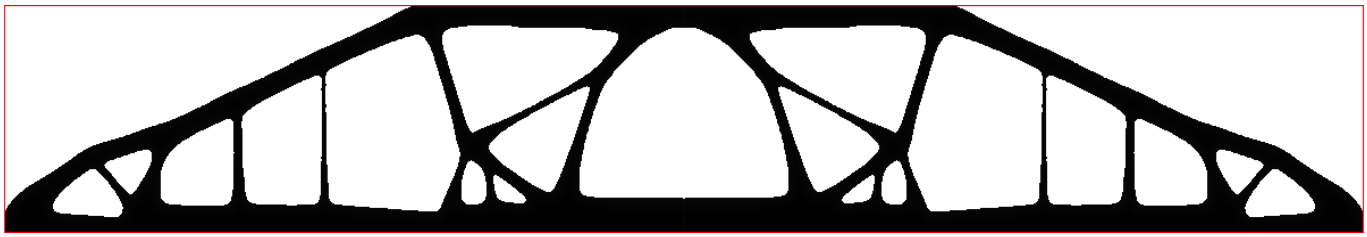

(d)

FIGURE 21. *Optimized shapes for the two-dimensional MBB Beam example of Section 5.3.3: (a) optimized shape Ω^* for Problem (5.3) (i.e. without additive manufacturing constraints), and optimized shapes for Problem (5.9) using parameters (b) $\alpha_c = 0.50$, (c) $\alpha_c = 0.30$, and (d) $\alpha_c = 0.10$.*

Let us observe, as in the two-dimensional bridge example of Section 5.3.2, that the optimized shapes still contain overhangs, which are concentrated on their upper regions, although the values of the mechanical constraint $P_{\text{sw}}(\Omega)$ are exactly the required ones (see Table 4). This suggests a flaw in the idea of penalizing the

Optimized shape	$J(\Omega)$	$\mathrm{Vol}(\Omega)$	$P_{\mathrm{sw}}(\Omega)$
Figure 21 (a)	68.57	0.899	7920
Figure 21 (b) ($\alpha_c = 0.50$)	71.38	0.900	3945
Figure 21 (c) ($\alpha_c = 0.30$)	74.41	0.900	2363
Figure 21 (d) ($\alpha_c = 0.10$)	84.59	0.900	791

TABLE 4. *Values of the compliance, the volume and the mechanical constraint $P_{\mathrm{sw}}(\Omega)$ for the optimized designs obtained in the 2d MBB Beam example of Section 5.3.3.*

overhang features of shapes owing to the functional $P_{\mathrm{sw}}(\Omega)$, which may be accounted for by two independent phenomena:

(1) As mentioned in Remark 4.1, the fact that each layer is assumed to be deposited instantaneously has an impact on the values of the self-weights c_{Ω_h} given by (4.2): the rigidity of completely flat overhangs (as those appearing in figures 21 (b)-(d)) is actually overestimated; roughly speaking, our modeling only involves the intermediate stages of the construction process where each layer is completely assembled, and where these flat regions are thereby connected to the lower structure. Hence, all the situations where these regions are hanging over void (for instance, at the moments when they are only half-constructed, and when the self-weight would take large values) are missed.

(2) Secondly, considering a uniform self-weight loading for each intermediate shape Ω_h leads to a concentration of the shape gradient of $J(\Omega)$ at regions closer to Γ_0. Intuitively, this comes from the fact that such regions appear in a greater number of intermediate shapes, which is reflected on the shape derivative of $P_{\mathrm{sw}}(\Omega)$; see Theorem 4.1. Thus, the algorithm favours the elimination of the overhangs located in these regions, while upper parts are comparatively less influenced by this requirement.

One remedy for the former issue would consist in using a more precise, 'pixel by pixel' model of the construction process introduced in Section 4.1: one could indeed consider the trajectory of the machine tool during the assembly of each layer of the shape, and take as 'intermediate shapes' several snapshots in the assembly of each layer. Unfortunately, beyond difficult modeling issues, relying on this idea would cause the computational cost (which is already significant) of the resulting constraint functional to increase dramatically. Therefore, this proposition is not examined in the present article.

A second remedy amounts to change the mechanical problem (4.1) characterizing the behavior of the intermediate shapes. More precisely, as proposed in Section 4.4, we consider fictitious body forces applied on the upper region of these shapes, thus better penalizing thin horizontal patterns in the intermediate shapes Ω_h. This is the purpose of the next section.

Last but not least, a third remedy consists in combining both informations from the geometric constraints of Section 3 and the mechanical constraint $P_{\mathrm{sw}}(\Omega)$. This possibility is examined in Section 5.5 below.

5.3.4. *Use of the modified manufacturing compliance $P_{\mathrm{uw}}(\Omega)$ in the two-dimensional bridge and MBB Beam examples.*

We now take on the two-dimensional bridge and MBB Beam examples of Sections 5.3.2 and 5.3.3, replacing the self-weight manufacturing compliance $P_{\mathrm{sw}}(\Omega)$ with the upper-weight manufacturing compliance $P_{\mathrm{uw}}(\Omega)$ in the formulation (5.9) of the optimization problem, with the expectation that it shows a better ability when it comes to removing overhanging features.

The thickness δ of the regions where g is applied in the definition (4.13) of the body force g_h is of the order of the mesh size: $\delta = \Delta x$.

In Figure 22, the optimized two-dimensional bridges obtained by using the upper-weight manufacturing compliance $P_{\mathrm{uw}}(\Omega)$ are represented, and the details about the various shapes are reported in Table 5. This modified constraint functional obviously shows a great efficiency in the reduction of overhangs. Note nevertheless that the volume constraint is not precisely satisfied in the case of Figure 22 (e) because the initialization does not sastify it and the algorithm cannot succeed to become feasible.

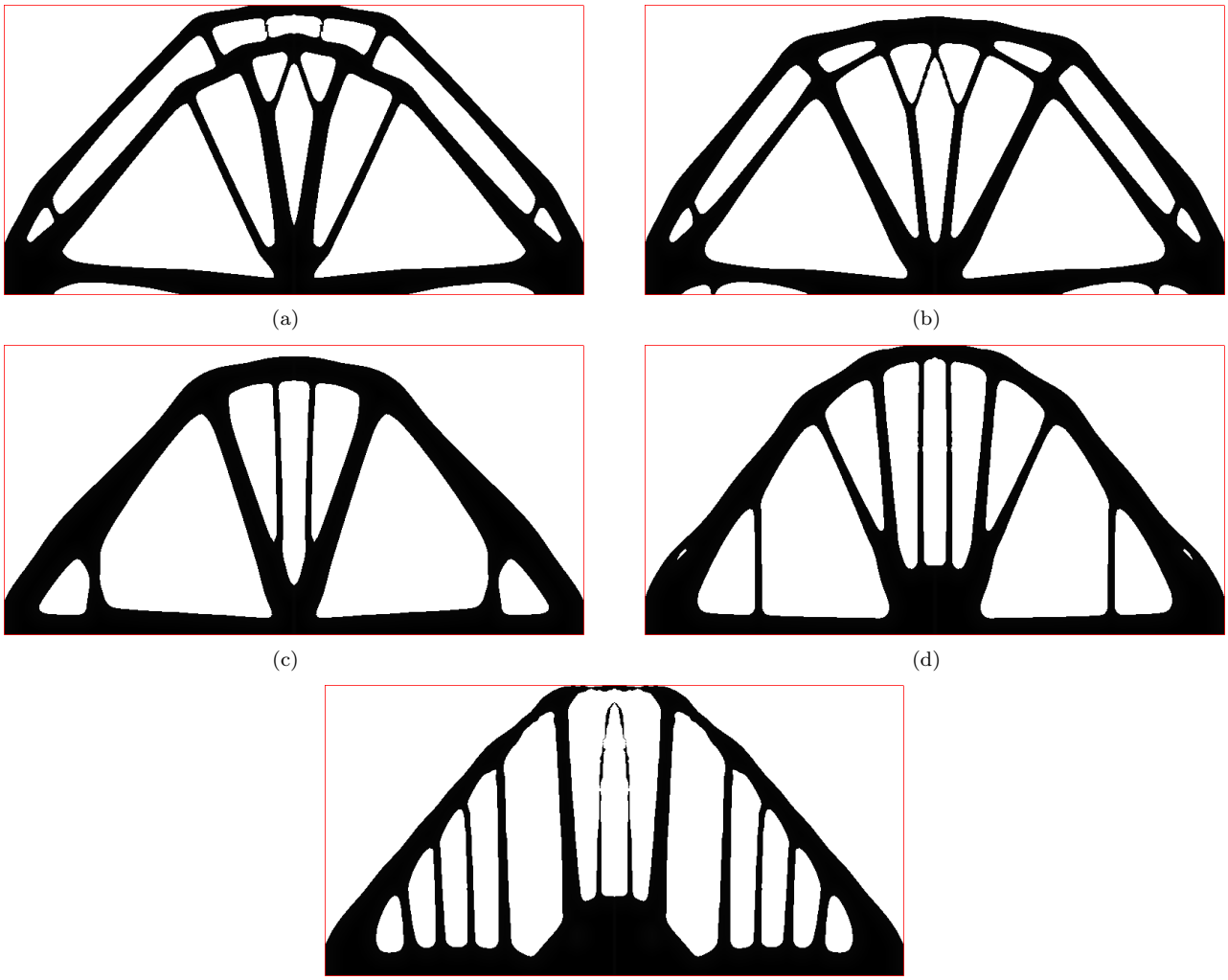

(a) (b) (c) (d) (e)

FIGURE 22. *Optimized two-dimensional bridges using the upper-weight manufacturing compliance* $P_{\mathrm{uw}}(\Omega)$*, and the parameters* $\alpha_v = 0.3$ *and (a)* $\alpha_c = 0.7$*, (b)* $\alpha_c = 0.5$*, (c)* $\alpha_c = 0.3$*, (d)* $\alpha_c = 0.2$*, and (e)* $\alpha_c = 0.1$*.*

Optimization design	$J(\Omega)$	$\mathrm{Vol}(\Omega)$	$P_{\mathrm{uw}}(\Omega)$
Figure 18 (right)	43.70	0.3	1.27
Figure 22 (a)	48.89	0.3	0.81
Figure 22 (b)	47.31	0.3	0.63
Figure 22 (c)	49.18	0.3	0.38
Figure 22 (d)	50.26	0.3	0.25
Figure 22 (e)	70.11	0.31	0.12

TABLE 5. *Values of the structural compliance, the volume and the upper-weight manufacturing compliance* $P_{uw}(\Omega)$ *for the optimized designs obtained in the* 2*d bridge example of Section 5.3.4.*

In Figure 23 we show the optimized shapes after the proposed substitution, in the two-dimensional MBB Beam example, for different values of α_c (and again $\alpha_v = 0.3$). The values of the involved functionals and

the convergence diagrams are shown in Table 6 and Figure 24 correspondingly. Note that, if some objective functions seem to increase at the beginning, it is because the volume constraint is not yet satisfied (it is ensured only at convergence).

One can observe that the algorithm tends to add more features oriented along the build direction and to connect them together by creating small archs, which have optimal rigidity for self-weight loadings. Again, the results are much more satisfying than those obtained by using the functional $P_{\text{sw}}(\Omega)$ when it comes to removing overhanging features.

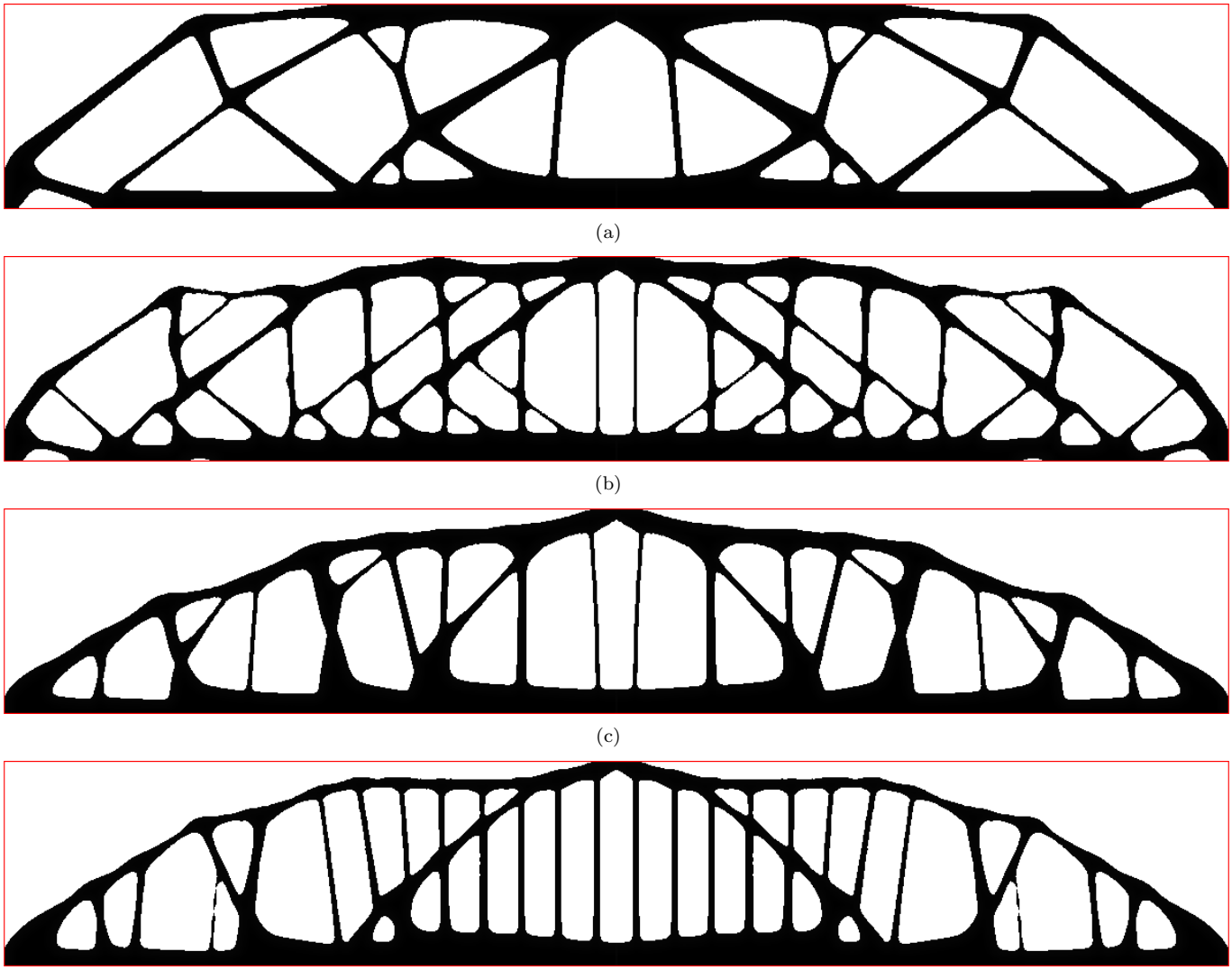

(a)

(b)

(c)

(d)

FIGURE 23. *Optimized shapes for the two-dimensional MBB Beam example of Section 5.3.3, solving Problem (5.9) with the upper-weight manufacturing compliance* $P_{\text{uw}}(\Omega)$ *and parameters (a)* $\alpha_c = 0.30$*, (b)* $\alpha_c = 0.10$*, (c)* $\alpha_c = 0.05$*, and (d)* $\alpha_c = 0.03$*.*

5.4. **Evaluation of the modified mechanical constraint functional** $P_{\text{uw}}(\Omega)$**.**

In the next subsections, we present several uses of the upper-weight manufacturing compliance $P_{\text{uw}}(\Omega)$.

Optimized shape	$J(\Omega)$	$\mathrm{Vol}(\Omega)$	$P_{\mathrm{uw}}(\Omega)$
Figure 23 (a)	68.57	0.899	60.00
Figure 23 (b) ($\alpha_c = 0.30$)	74.96	0.900	18.00
Figure 23 (c) ($\alpha_c = 0.10$)	89.42	0.899	5.93
Figure 23 (d) ($\alpha_c = 0.05$)	98.90	0.900	2.99

TABLE 6. *Values of the compliance, the volume and the upper-weight manufacturing compliance $P_{\mathrm{uw}}(\Omega)$ for the optimized designs obtained in the 2d MBB Beam example of Section 5.3.3.*

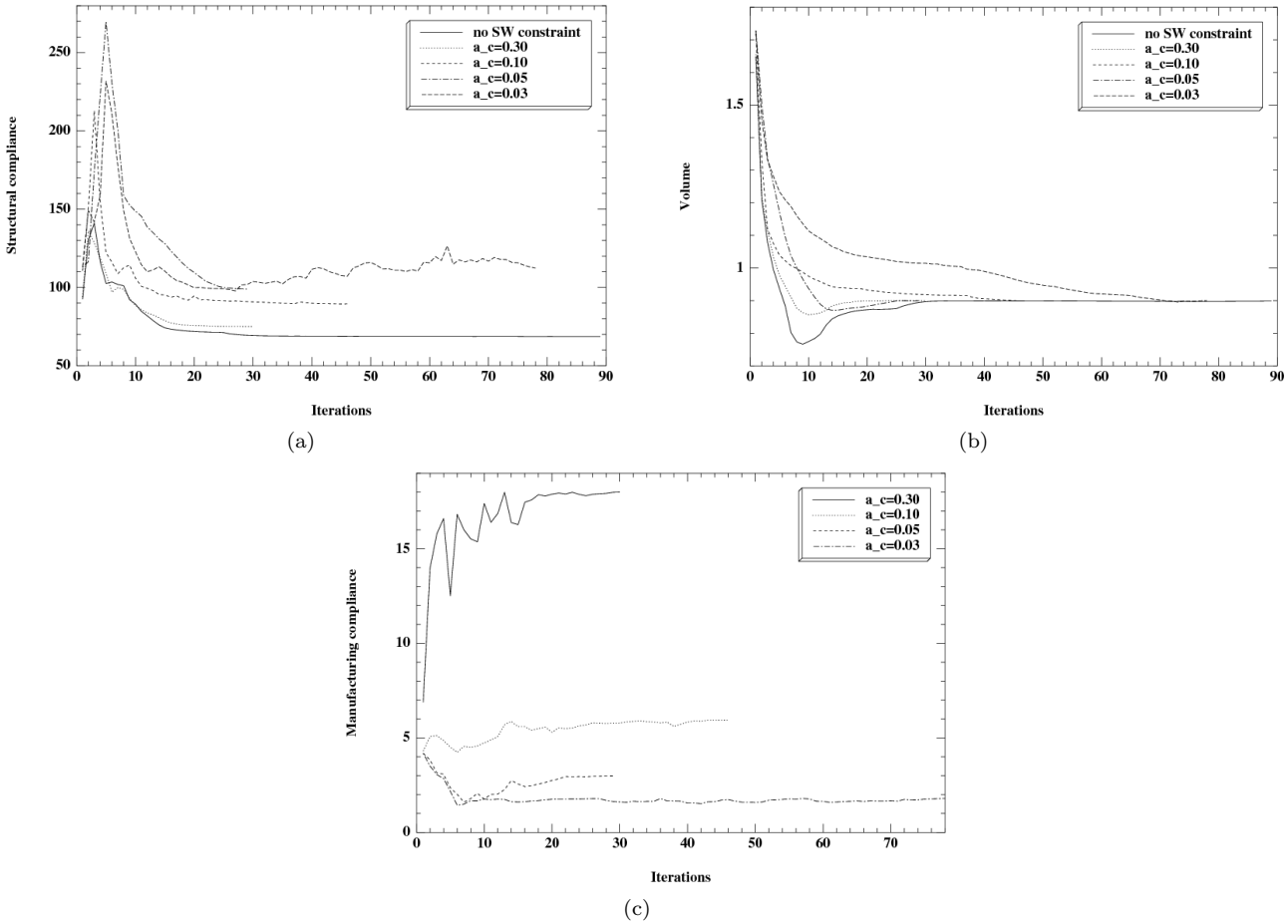

FIGURE 24. *Convergence histories associated to the two-dimensional MBB Beam optimization example of Section 5.3.3, leading to the optimized shapes in Figure 23: (a) structural compliance $J(\Omega)$, (b) volume $\mathrm{Vol}(\Omega)$, and (c) upper-weight manufacturing compliance $P_{\mathrm{uw}}(\Omega)$.*

5.4.1. *Three-dimensional cantilever beam.*

Our first three-dimensional example is a cantilever beam with size $0.5 \times 0.5 \times 1$, clamped at its bottom side and subjected to a unit load $f = (1, 0, 0)$ applied at the middle of its upper side; see Figure 25. The shape is assembled from bottom to top, and so Γ_0 and Γ_D coincide. Due to the symmetry of the mechanical problem, the calculations are performed on only half the computational domain D. The associated Cartesian grid $\mathcal{G}$ is composed of $20 \times 40 \times 80$ elements.

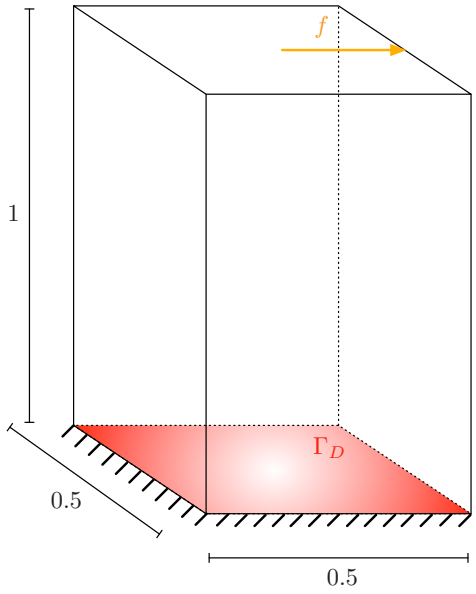

FIGURE 25. *Setting of the three-dimensional cantilever test case.*

Starting with a full domain initialization, we solve the compliance minimization problem under volume constraint (5.3) for $\alpha_v = 0.075$, which yields the optimized shape Ω^* displayed on Figure 26 (a).

The shape Ω^* presents four overhanging bars; so as to obtain a three-dimensional cantilever without such features, we start the optimization anew, adding a constraint on the upper-weight manufacturing compliance, i.e. we solve:

$$\begin{array}{ll} \min\limits_{\Omega} & J(\Omega) \\ \text{s.t.} & \mathrm{Vol}(\Omega) \leq \alpha_v \mathrm{Vol}(D), \\ & P_{\mathrm{uw}}(\Omega) \leq \alpha_c P_{\mathrm{uw}}(\Omega^*), \end{array} \tag{5.11}$$

for the values $\alpha_v = 0.075$ and $\alpha_c = 0.90$, then $\alpha_c = 0.70$. Again, the 0^{th}-order procedure is used for the calculations of $P_{\mathrm{uw}}(\Omega)$ and its derivative, with $N = 40$ evenly distributed layers. This results in the optimized shapes displayed on Figures 26 (b) and (c), where the overhanging bars have disappeared. Table 7 and Figure 27 supply information about the values of the involved criteria, as well as their evolution during the optimization. Note that the upper-weight manufacturing compliance is much smaller than the final use compliance because of different orders of magnitude of the applied loads.

Optimized design	$J(\Omega)$	$\mathrm{Vol}(\Omega)$	$P_{\mathrm{uw}}(\Omega)$
Figure 26 (a)	1918	0.0093	8.33e-06
Figure 26 (b) ($\alpha_c = 0.90$)	1982	0.0093	7.20e-06
Figure 26 (c) ($\alpha_c = 0.70$)	2047	0.0093	5.78e-06

TABLE 7. *Values of the compliance, the volume and the upper-weight manufacturing compliance $P_{\mathrm{uw}}(\Omega)$ for the optimized designs obtained in the 3d cantilever test case of Section 5.4.1.*

5.4.2. *Three-dimensional bridge.*

The next example is a three-dimensional version of the bridge example of Section 5.3.2, as depicted in Figure 28: the dimensions of the working domain D are $6 \times 1 \times 1$. The structure is clamped at its lower-right corners, while at its lower-left corners, the vertical displacement is prevented. A uniform load $f = (0, 0, -1)$

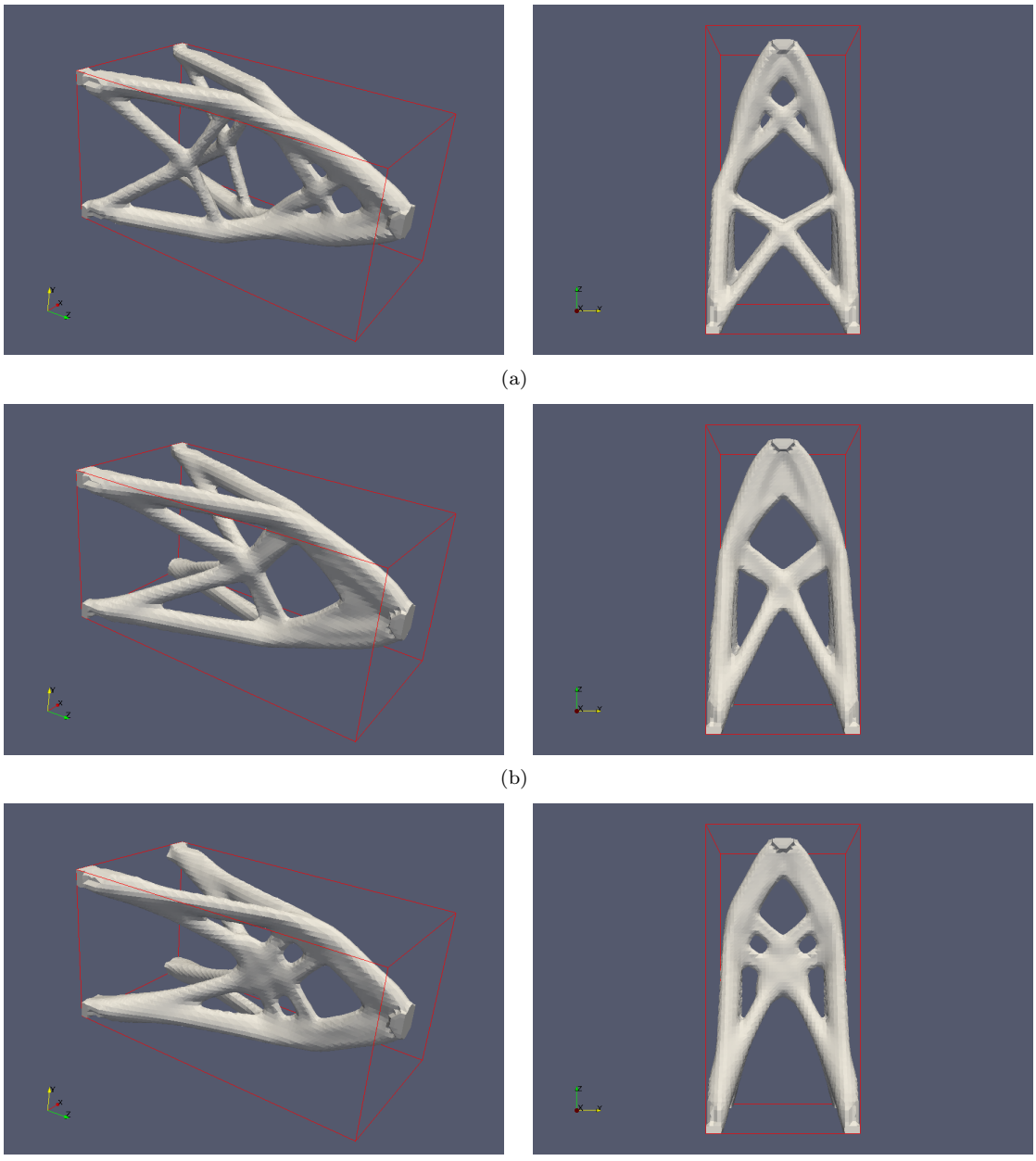

FIGURE 26. *Optimized three-dimensional cantilever in the test-case of Section 5.4.1, solving Problem (5.11) (a) without additive manufacturing constraints, (b) using* $\alpha_c = 0.90$*, and (c) using* $\alpha_c = 0.70$.

is applied on the upper side of the structure. From the manufacturing point of view, the shape is constructed from *top to bottom*, i.e. Γ_0 coincides with the upper side of D (i.e. the deck of the bridge). Due to the double symmetry of the mechanical problem, only one quarter of D is meshed and the cubic grid $\mathcal{G}$ is composed of $90 \times 15 \times 30$ elements.

We start by minimizing the structural compliance $J(\Omega)$ of the bridge under volume constraint, taking the full working domain D as initial shape; i.e. we solve (5.3) with $\alpha_v = 0.10$. Figure 29 (left column) shows the resulting optimized shape Ω^*, which presents several overhangs of significant structural importance.

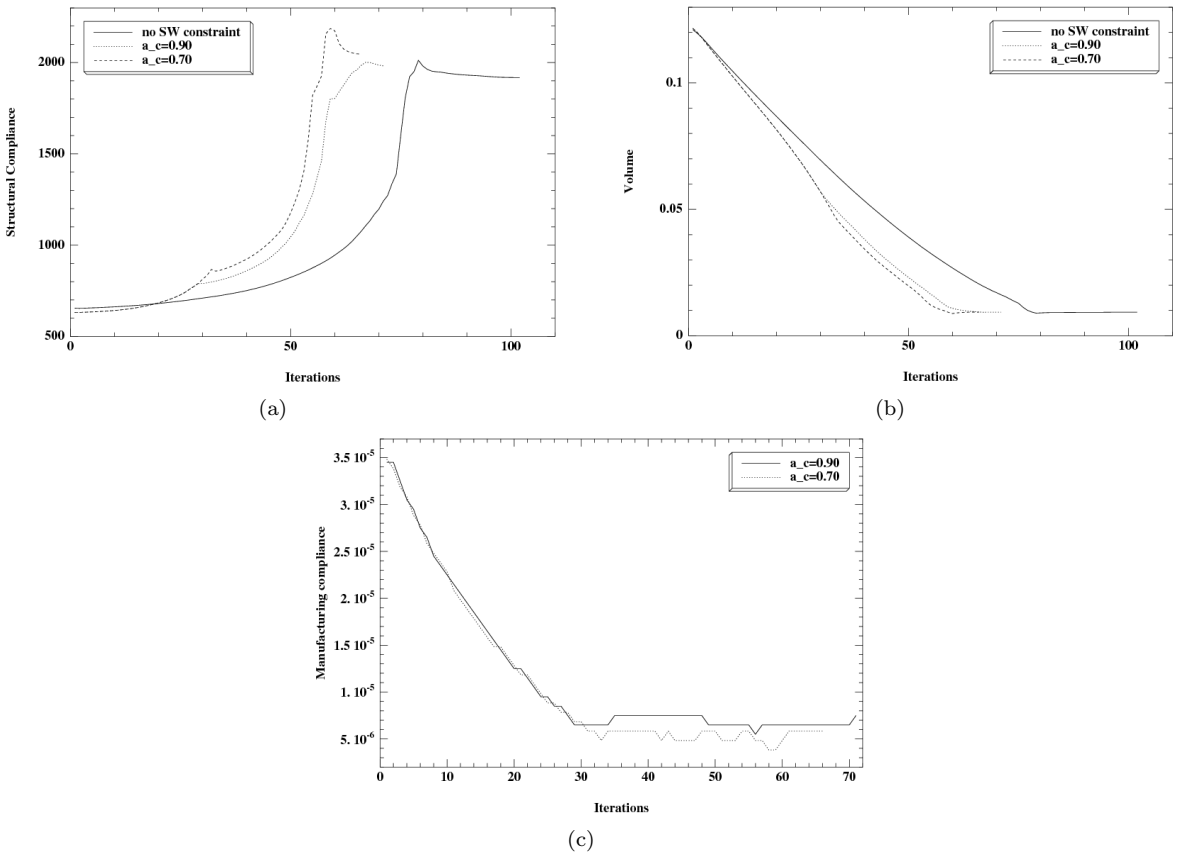

FIGURE 27. *Convergence histories for the optimized three-dimensional cantilever beams of Figure 26: (a) structural compliance $J(\Omega)$, (b) volume* $\mathrm{Vol}(\Omega)$*, and (c) upper-weight manufacturing compliance* $P_{\mathrm{uw}}(\Omega)$.

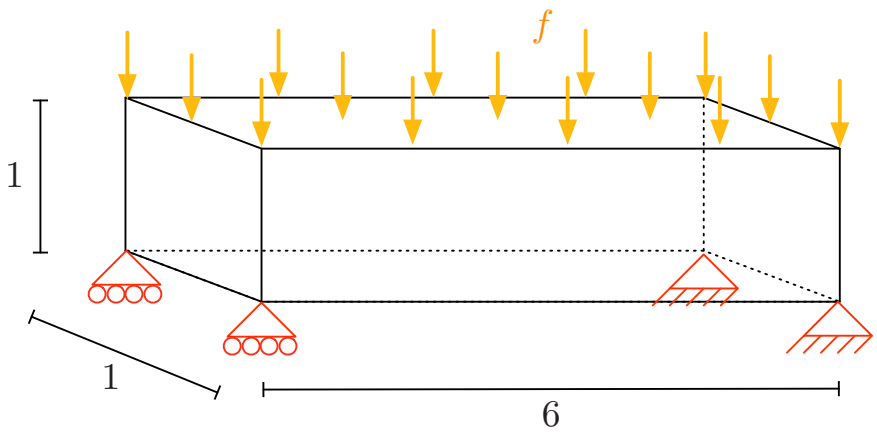

FIGURE 28. *Setting of the three-dimensional bridge test-case.*

We then add a constraint on the upper-weight manufacturing compliance $P_{\mathrm{uw}}(\Omega)$, but instead of solving (5.11) we rather consider the following optimization problem:

$$\begin{aligned} \min_{\Omega} \quad & \mathrm{Vol}(\Omega), \\ \text{s.t.} \quad & J(\Omega) \leq J(\Omega^*), \\ & P_{\mathrm{uw}}(\Omega) \leq \alpha_c P_{\mathrm{uw}}(\Omega^*), \end{aligned} \tag{5.12}$$

where we look for a shape having at least the same rigidity as Ω^*, but which is also more rigid from a manufacturing perspective (it is therefore expected that the volume $\mathrm{Vol}(\Omega)$ is greater than $\mathrm{Vol}(\Omega^*)$). Figures 29 (right column) and 30 (left column) show the optimized shapes for $\alpha_c = 0.70$ and $\alpha_c = 0.10$ respectively. For $\alpha_c = 0.70$ only slight changes are observed: the upper bar becomes thinner and the central bars become thicker and are relocated closer to Γ_0. For $\alpha_c = 0.10$ the changes are drastic and the same trend as in the two-dimensional MBB beam is observed. Table 8 and Figure 31 contain the values and the evolution history of the involved functionals. Interestingly, the shape of Figure 29 (right column) is better compared to that of Figure 29 (left column) with respect to all criteria (i.e. volume, structural and manufacturing compliances), indicating the existence of several local minimizers for Problem (5.3).

Observe however that the resulting shapes still contain (small) overhangs (see the upper regions of the shapes in Figures 29 and 30). These suggest that the upper-weight manufacturing compliance constraint $P_{\mathrm{uw}}(\Omega)$ is a valuable tool in preventing overhanging features, but that it still suffers from the assumption of instantaneous layer deposition described in Remark 4.1.

Optimized shape	$J(\Omega)$	$\mathrm{Vol}(\Omega)$	$P_{\mathrm{uw}}(\Omega)$
Figure 29 (left)	7724800	0.150	4.542e-03
Figure 29 (right) ($\alpha_c = 0.7$)	7697520	0.149	2.967e-03
Figure 30 (left) ($\alpha_c = 0.1$)	7575730	0.170	0.424e-03

TABLE 8. *Values of the compliance, the volume and the upper-weight manufacturing compliance $P_{\mathrm{uw}}(\Omega)$ for the optimized three-dimensional bridges of figures 29 and 30.*

One last observation concerns the purely three-dimensional phenomenon examplified on Figure 30 (right column): for decreasing values of α_c the optimized shapes show, at each level, sufficient support from the lower structure to enable their manufacturability. However, there is no information about *where* this support comes from. More precisely, the shape could be self-supporting assuming that the printing direction of each layer is directed along the x-axis, but not when it is printed along the y-axis, as in the example proposed in Figure 32. This effect is another shortcoming of our simplified modeling of the construction process, which does not take into account the printing path of each individual layer; see Remark 4.1. Notice that it similarly plagues the purely geometric constraints introduced in Section 3.

5.5. **Mixing geometric and mechanical criteria.**

As we have mentioned in Section 5.3.3, mixing geometric and mechanical criteria is a possible remedy to the artifacts caused by the assumption of an instantaneous assembly of each layer during the construction process. A first idea in this direction consists in introducing a new version of the system (4.1) or (4.14) involving a volume or surface load related to the orientation of the structural boundary.

A second possibility is to combine the geometric functionals of Section 3 with the mechanical functionals of Section 4; in this spirit, we may now solve, for instance, the optimization problem:

$$\begin{array}{ll} \min\limits_{\Omega} & (1-\alpha_g)\dfrac{J(\Omega)}{J(\Omega^*)} + \alpha_g \dfrac{P_a(\Omega)}{P_a(\Omega^*)}, \\ \text{s.t.} & \mathrm{Vol}(\Omega) \leq \alpha_v \mathrm{Vol}(D), \\ & P_{\mathrm{uw}}(\Omega) \leq \alpha_c P_{\mathrm{uw}}(\Omega^*), \end{array} \tag{5.13}$$

where α_v, α_c and α_g are in $[0,1]$. Both strategies are quite similar in essence. We have implemented both and the obtained results follow a similar logic. For brevity, we present only the second method in this work.

Remark 5.2. *The choice of an initial shape for the optimization problem (5.13) is crucial in applications. The natural idea is to start from a rather arbitrary initial shape (as in the previous examples), which gives more freedom to the algorithm. As we have explained in Section 5.2.2, doing so may however increase the risk that the optimization process fall into a local minimum.*

Another idea is to take as initial shape for (5.13) the already optimized shape for Problem (5.11) or (5.12). This may facilitate the optimization process if there are no horizontal features of critical importance for the

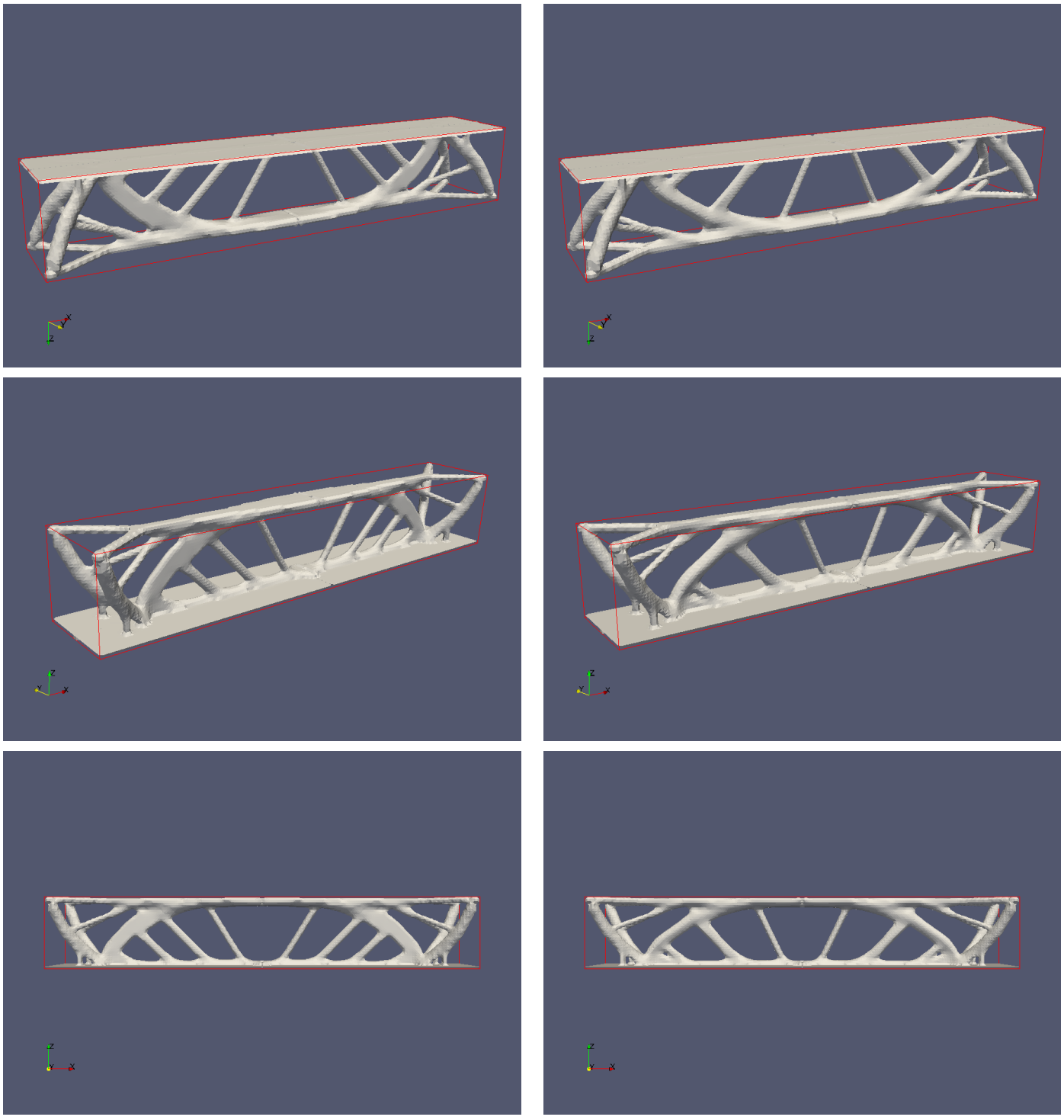

FIGURE 29. *Optimized designs for the three-dimensional bridge example of Section 5.4.2, (left) without manufacturing constraints, (right) solving Problem (5.12) with* $\alpha_c = 0.7$.

overall structural performance. Else, having less freedom to change the loading path, it may be difficult for the algorithm to find a compromise between the two criteria. Therefore, we believe that the choice of an adequate initial shape for problem (5.13) is case dependent.

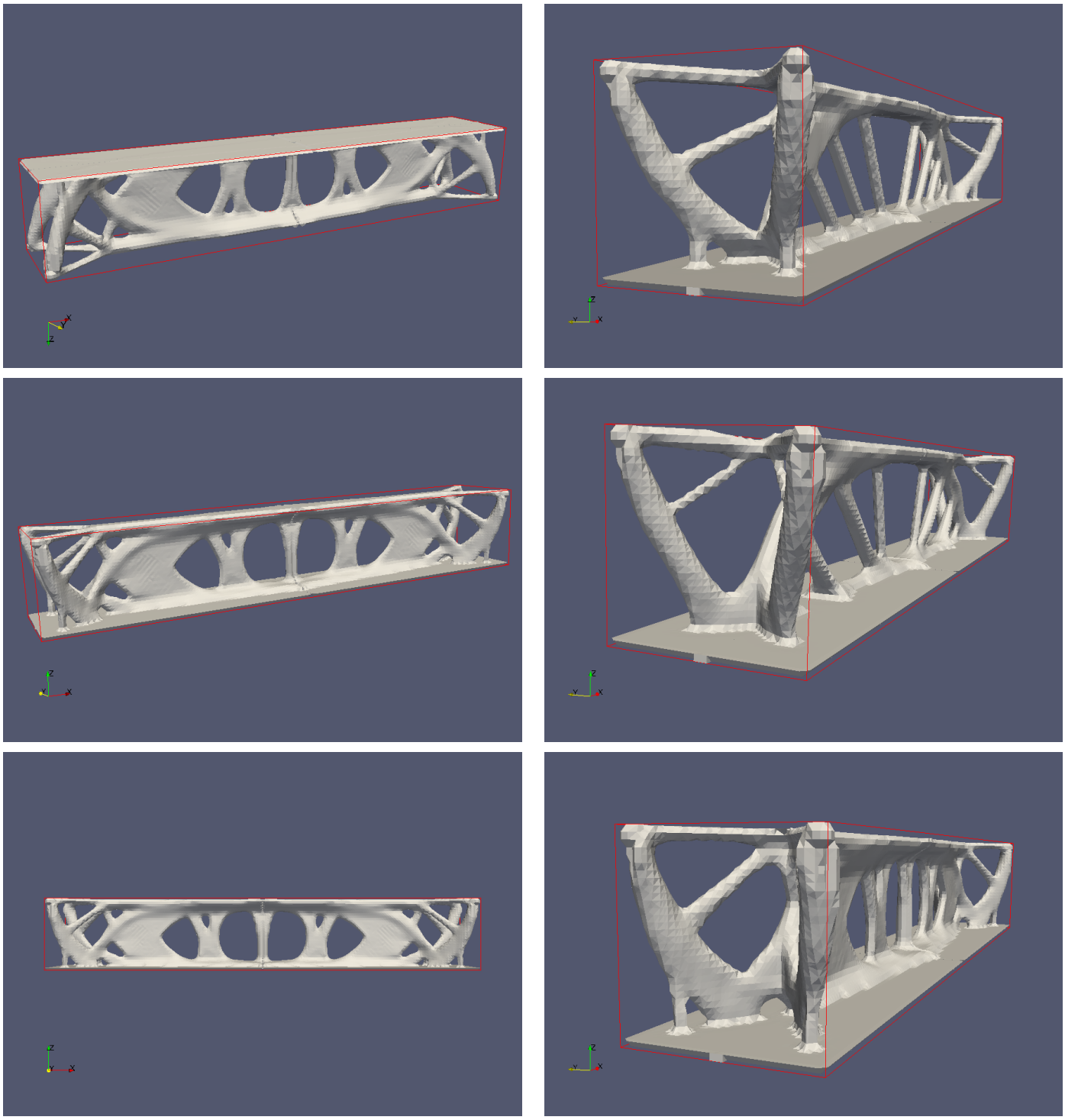

FIGURE 30. *(Left) Different views of the optimized shape for the three-dimensional bridge example of Section 5.4.2, solving Problem (5.12) with* $\alpha_c = 0.1$*; (right) another view on the three-dimensional bridges for Problem (5.12) with (top) no manufacturing constraint, (middle)* $\alpha_c = 0.7$ *and (bottom)* $\alpha_c = 0.1$.

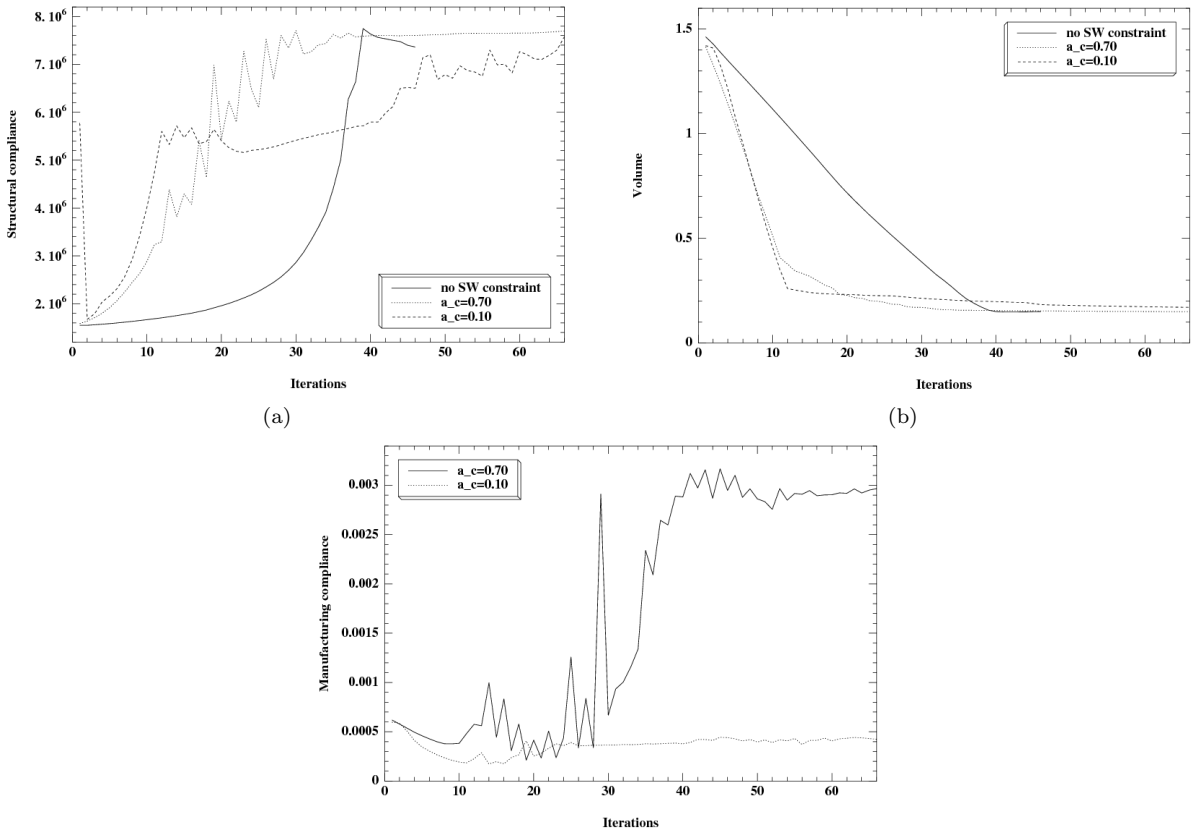

FIGURE 31. *Convergence histories for the three-dimensional bridges of Figures 29 (right) and 30; (a) structural compliance $J(\Omega)$, (b) volume* $\mathrm{Vol}(\Omega)$*, and (c) upper-weight manufacturing compliance $P_{\mathrm{uw}}(\Omega)$.*

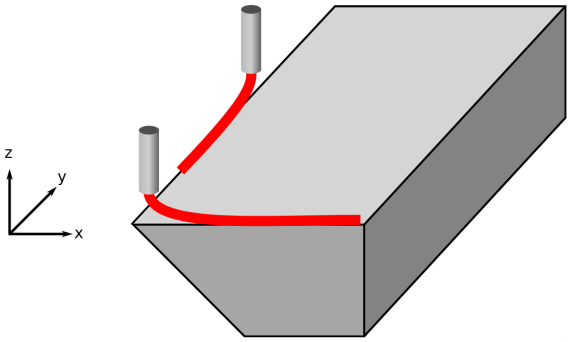

FIGURE 32. *Example of a feature which is self-supporting when each layer is assembled following the x direction, but not when it is assembled following the y direction.*

5.5.1. *Two-dimensional MBB beam.*

Let us consider again the two-dimensional MBB beam example of Section 5.3.3. Starting from the optimized shape of Figure 23 (c), we aim to improve the angle between the structural boundary and the (vertical) build direction by solving the optimization problem (5.13), with a threshold value $\nu = 45°$. In Figure 33 we

show the results for different values of the weight α_g. As is examplified in Table 9, larger values of α_g results in smaller values of $P_a(\Omega)$, at the expense of a deteriorated structural compliance $J(\Omega)$.

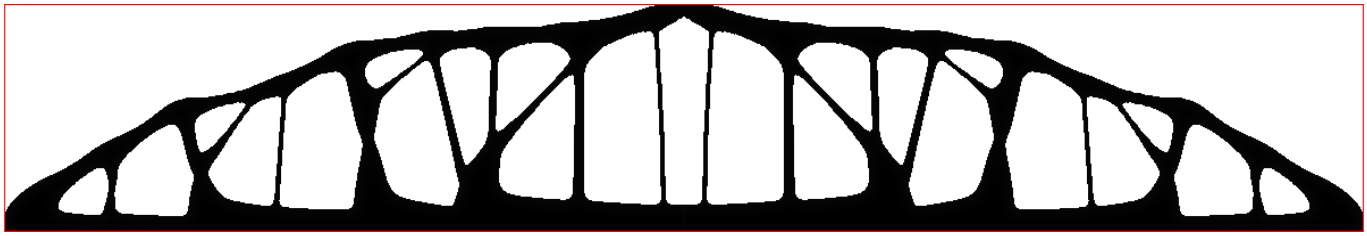

(a)

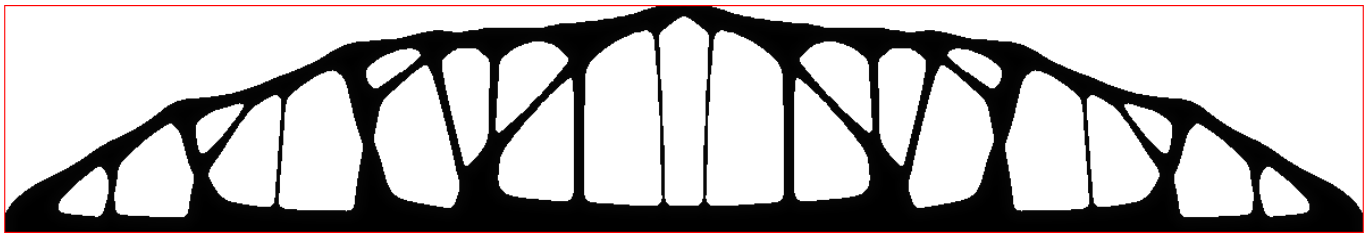

(b)

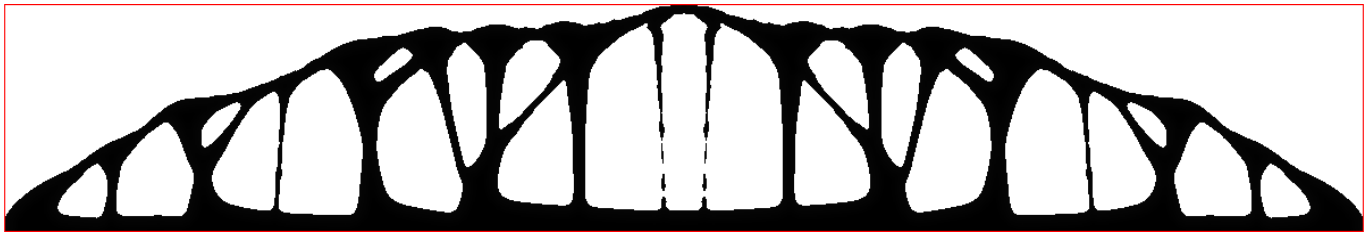

(c)

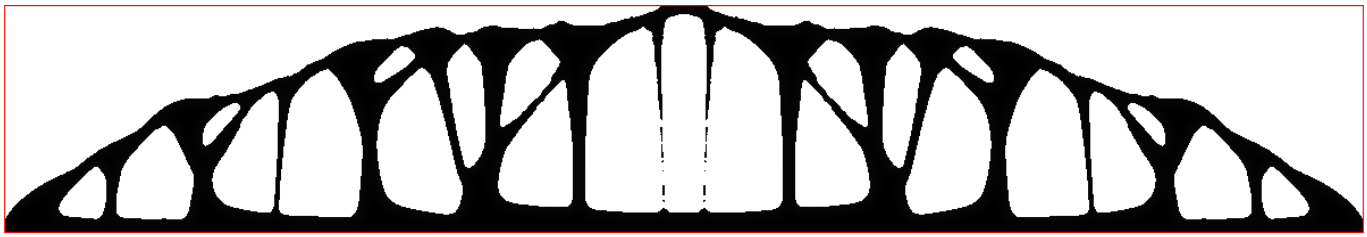

(d)

FIGURE 33. *Optimized two-dimensional MBB Beams resulting from the mixed shape optimization problem (5.13) in Section 5.5.1, with the parameters: (a) $\alpha_g = 0$, $\alpha_c = 0.05$, (b) $\alpha_g = 0.10$, $\alpha_c = 0.05$, (c) $\alpha_g = 0.30$, $\alpha_c = 0.05$, and (d) $\alpha_g = 0.50$, $\alpha_c = 0.05$.*

Optimized shape	$J(\Omega)$	Vol(Ω)	$P_{\text{uw}}(\Omega)$	$P_a(\Omega)$	Iterations for Problem (5.13)
Figure 33 (a)	98.90	0.900	2.99	0.105	-
Figure 33 (b)	100.36	0.900	2.98	0.076	16
Figure 33 (c)	116.73	0.900	2.76	0.043	18
Figure 33 (d)	121.79	0.899	2.91	0.038	20

TABLE 9. *Values of the various shape functionals involved in the resolution of Problem (5.13) in the context of the two-dimensional MBB Beam of Section 5.5.1.*

Remark 5.3. *From the results in Figure 33, one may get the erroneous impression that the two vertical bars at the centre are disconnected from the structure. In fact, what we actually plot in all the above results is the* 0 *isovalue of the level set function associated to the shape. Thus, thin features of the size of the computational mesh* $\mathcal{G}$ *may look disconnected. However, recall that the Finite Element resolution of the linearized elasticity systems (2.1) relies on the 'ersatz material' approximation, whereby the mechanical properties of the elements intersected by the structural boundary are endowed intermediate values between those of the 'bulk' material occupying* Ω *and the material simulating void. To make this point clearer, in Figure 34 we plot both the* 0 *isovalue of the level set function and the corresponding distribution of the Young's modulus for the shape of Figure 33 (d). One observes that the Young's modulus takes intermediate values at the regions that appear disconnected (and so, they retain some rigidity).*

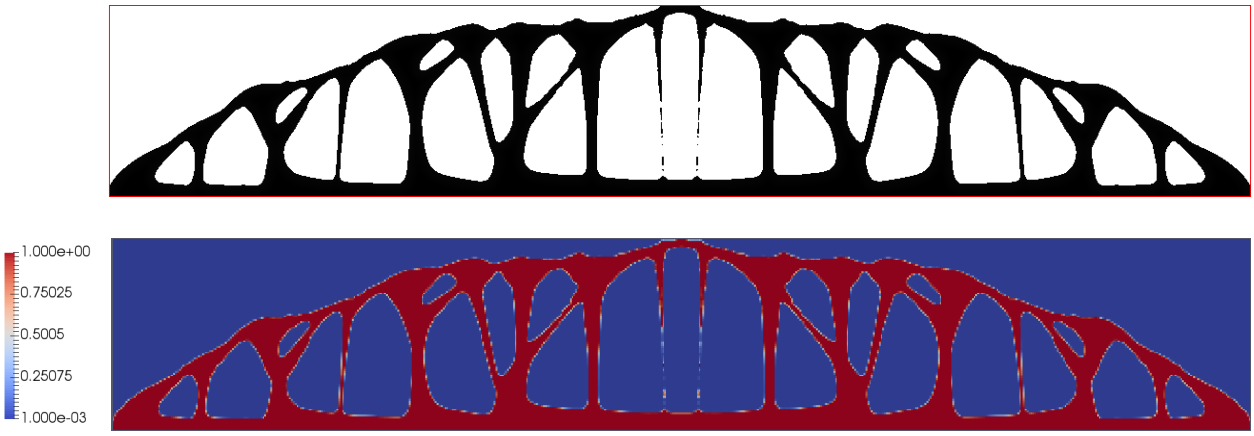

FIGURE 34. *(Top) negative subdomain of the level set function associated to the optimized shape in Figure 33, (d), and (bottom) the distribution of the Young's modulus in the computational domain* D.

5.5.2. *Three-dimensional bridge.*

We now consider the three-dimensional bridge test-case of section 5.4.2, whose details are reported on Figure 28. We consider the following optimization problem:

$$\begin{aligned} \min_{\Omega} \quad & (1-\alpha_g)\frac{\mathrm{Vol}(\Omega)}{\mathrm{Vol}(\Omega^*)} + \alpha_g \frac{P_a(\Omega)}{P_a(\Omega^*)}, \\ \text{s.t.} \quad & J(\Omega) \leq J(\Omega^*) \\ & P_{\mathrm{uw}}(\Omega) \leq \alpha_c P_{\mathrm{uw}}(\Omega^*), \end{aligned} \tag{5.14}$$

where the parameters α_c and α_g are in $[0,1]$, and the reference shape Ω^* is the optimized shape for Problem (5.3), depicted in Figure 29 (left). Due to the existence of some nearly flat overhanging parts in the results of section 5.4.2 close to the anchor points, we initialize Problem (5.14) with the full computational domain D for this example.

The optimized shape associated to the parameters $\alpha_c = 0.70$, $\alpha_g = 0.10$ is represented on Figure 35. The shape differs significantly from that of Figure 29 (right column), where no angle penalization was used. It is also interesting to note that the manufacturing compliance of the shape has been significantly reduced, at the expense of a very slight volume increase (see Table 10).

Still starting from the full domain D, Figure 36 (left and right columns) depicts the optimized shapes for the parameters $\alpha_c = 0.10$, $\alpha_g = 0.10$ and $\alpha_c = 0.10$, $\alpha_g = 0.90$ respectively. From Table 11, where the values of the shape functionals of interest are reported, it is interesting to note that the choice $\alpha_c = 0.10$, $\alpha_g = 0.10$ leads to a design that performs worse than that of Figure 30, both in terms of manufacturing compliance and angle violation, but which has a much smaller volume, once more validating the intuition that the problem has many local minimizers. Moreover, we observe that a severe penalization of the regions

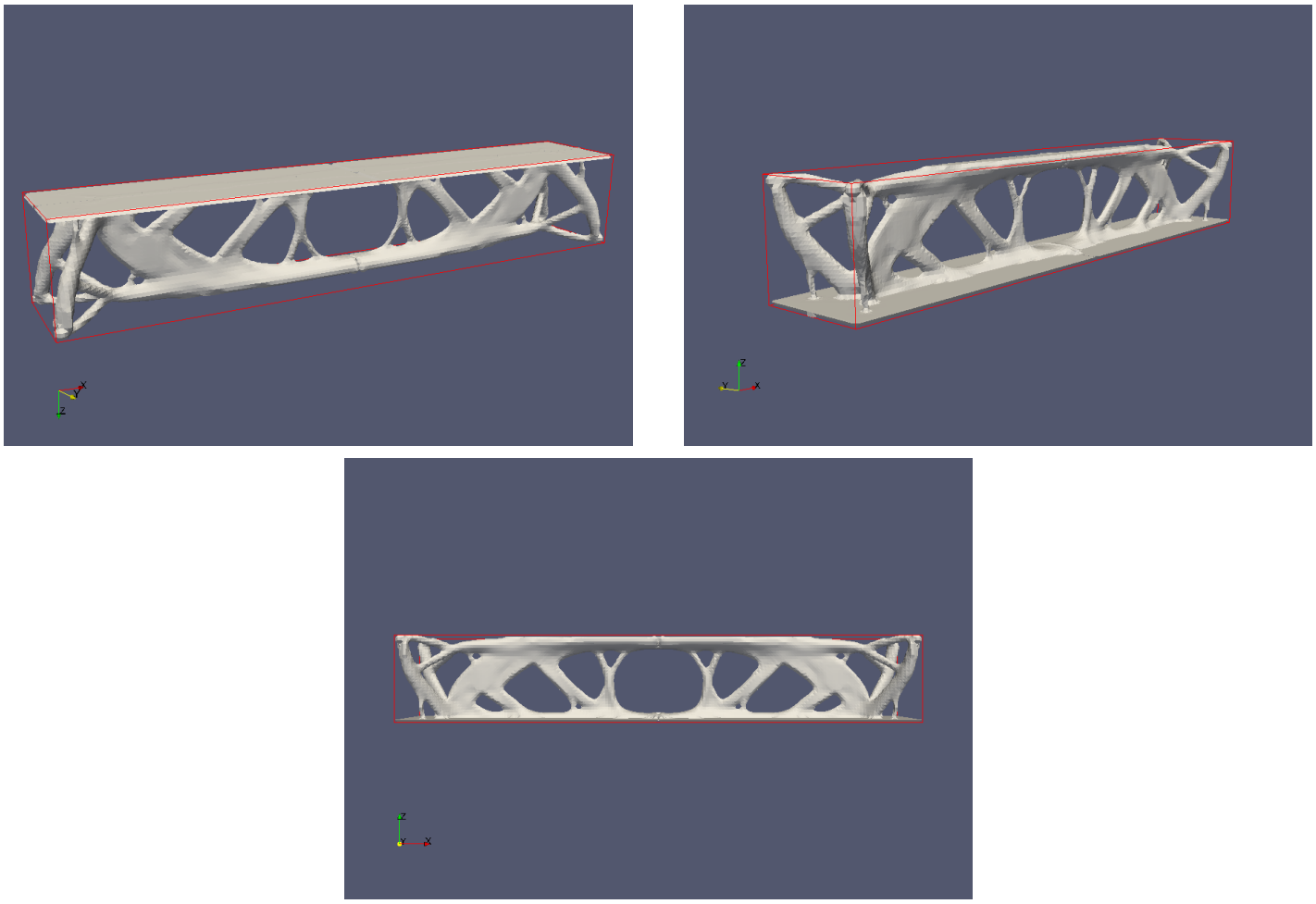

FIGURE 35. *Optimized shape for the three-dimensional bridge example for the combined geometrically and mechanically constrained Problem (5.14) setting* $\alpha_c = 0.70$, $\alpha_g = 0.10$.

Optimized shape	$J(\Omega)$	$\mathrm{Vol}(\Omega)$	$P_{\mathrm{uw}}(\Omega)$	$P_a(\Omega)$	Iterations
Figure 29 (right column)	7697520	0.149	2.967e-03	0.0235	84
Figure 35	7719590	0.151	0.958e-03	0.0176	44

TABLE 10. *Values of the compliance, the volume, the upper-weight manufacturing compliance* $P_{\mathrm{uw}}(\Omega)$ *and the geometric constraint* $P_a(\Omega)$ *for the optimized* 3*d bridges of figures 29 (right column) and 35.*

violating the imposed threshold angle lead to significant changes of the shape. In Figure 36 (right column) we see that the previous nearly flat overhangs do not appear anymore and the new structural system uses significantly greater volume to abide by the compliance criterion (see Table 11).

Acknowledgements. G. A. is a member of the DEFI project at INRIA Saclay Ile-de-France; the work of C.D. is partially supported by the IRS-CAOS grant from Université Grenoble-Alpes.

REFERENCES

[1] S. AHN, M. MONTERO, D. ODELL, S. ROUNDY, AND P. WRIGHT, *Anisotropic material properties of fused deposition modeling abs*, Rapid Prototyping Journal, 8 (2002), pp. 248–257.

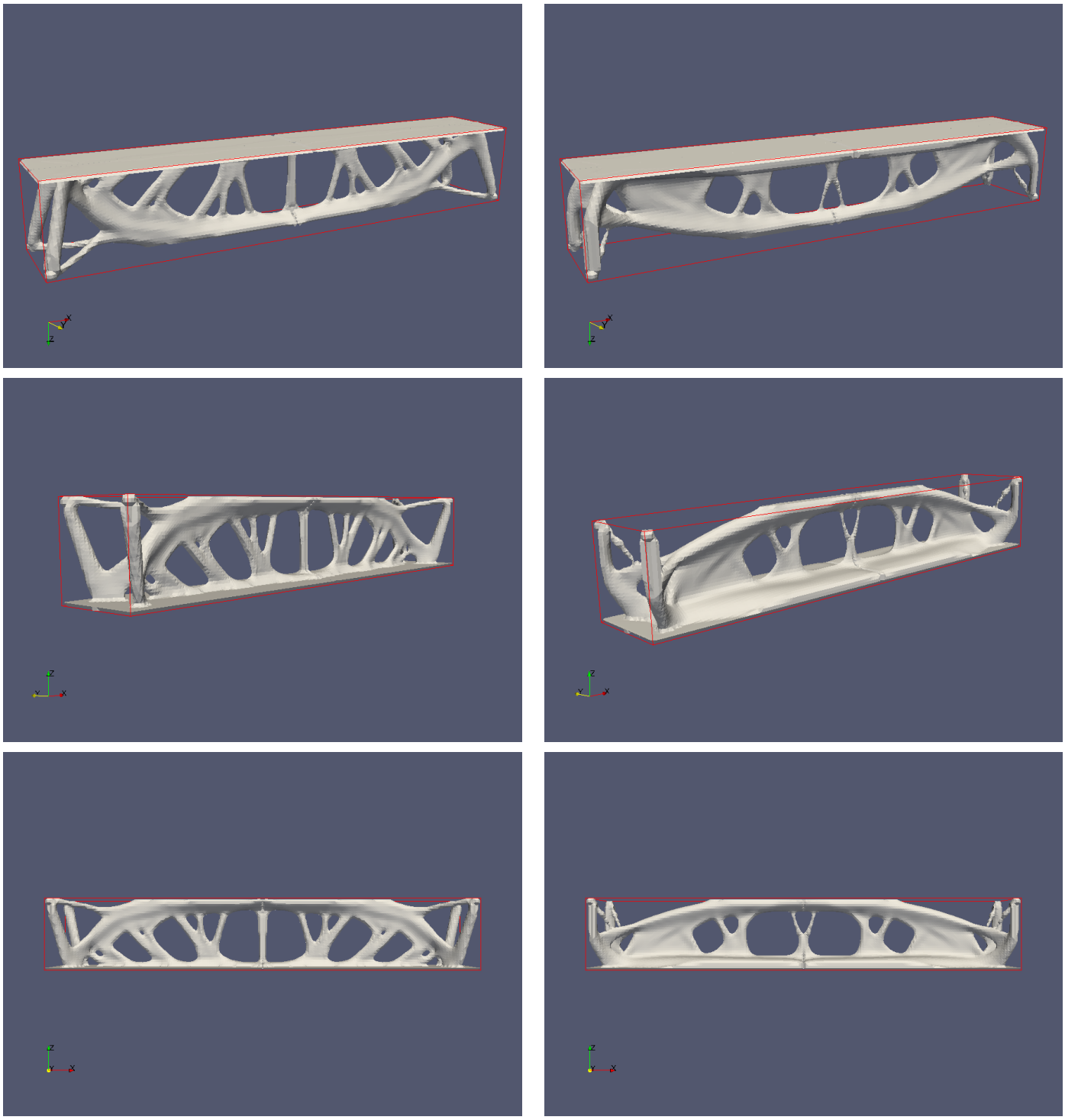

FIGURE 36. *Optimized three-dimensional bridges for the combined geometrically and mechanically constrained Problem (5.14) setting (left)* $\alpha_c = 0.10$, $\alpha_g = 0.10$, *and (right)* $\alpha_c = 0.10$, $\alpha_g = 0.90$.

[2] G. ALLAIRE, *Conception optimale de structures*, vol. 58 of Mathématiques & Applications (Berlin), Springer-Verlag, Berlin, 2007.

Optimized shape	$J(\Omega)$	$\mathrm{Vol}(\Omega)$	$P_{\mathrm{uw}}(\Omega)$	$P_a(\Omega)$	Iterations
Figure 30	7575730	0.170	0.424e-03	0.013	92
Figure 36 (left column), $\alpha_c = 0.1$, $\alpha_g = 0.1$	7704890	0.154	0.448e-03	0.014	55
Figure 36 (right column), $\alpha_c = 0.1$, $\alpha_g = 0.9$	7538300	0.282	0.437e-03	0.005	43

TABLE 11. *Values of the compliance, the volume, the upper-weight manufacturing compliance $P_{\mathrm{uw}}(\Omega)$ and the geometric constraint $P_a(\Omega)$ for the optimized 3d bridges of Figures 30 and 36 (left and right columns).*

[3] G. Allaire, C. Dapogny, A. Faure, and G. Michailidis, *Shape optimization of a layer by layer mechanical constraint for additive manufacturing*, HAL preprint: https://hal.archives-ouvertes.fr/hal-01398877, (2016).

[4] G. Allaire and L. Jakabcin, *Taking into account thermal residual stresses in topology optimization of structures built by additive manufacturing*, (in preparation), (2017).

[5] G. Allaire, F. Jouve, and A.-M. Toader, *Structural optimization using sensitivity analysis and a level-set method*, Journal of computational physics, 194 (2004), pp. 363–393.

[6] C. Barlier and A. Bernard, *Fabrication additive - Du Prototypage Rapide l'impression 3D*, Dunot, 2015.

[7] M. Bendsoe and O. Sigmund, *Topology optimization: theory, methods and applications*, Springer, 2004.

[8] D. Brackett, I. Ashcroft, and R. Hague, *Topology optimization for additive manufacturing*, in Proceedings of the Solid Freeform Fabrication Symposium, Austin, TX, 2011, pp. 348–362.

[9] S. Cacace, E. Cristiani, and L. Rocchi, *A level set based method for fixing overhangs in 3d printing*, Applied Mathematical Modelling, (2017), pp. 446–455.

[10] F. Calignano, *Design optimization of supports for overhanging structures in aluminum and titanium alloys by selective laser melting*, Materials & Design, 64 (2014), pp. 203–213.

[11] S. L. Campbell, J.-P. Chancelier, and R. Nikoukhah, *Modeling and Simulation in SCILAB*, Springer, 2006.

[12] A. Clausen, *Topology optimization for additive manufacturing*, (2016).

[13] D. E. Cooper, M. Stanford, K. A. Kibble, and G. J. Gibbons, *Additive manufacturing for product improvement at red bull technology*, Materials & Design, 41 (2012), pp. 226–230.

[14] C. Dapogny, A. Faure, G. Michailidis, G. Allaire, A. Couvelas, and R. Estevez, *Geometric constraints for shape and topology optimization in architectural design*, Computational Mechanics, (2017).

[15] P. Das, R. Chandran, R. Samant, and S. Anand, *Optimum part build orientation in additive manufacturing for minimizing part errors and support structures*, Procedia Manufacturing, 1 (2015), pp. 343–354.

[16] J. Dumas, J. Hergel, and S. Lefebvre, *Bridging the gap: automated steady scaffoldings for 3d printing*, ACM Transactions on Graphics (TOG), 33 (2014), p. 98.

[17] P. Dunning and H. Kim, *Introducing the sequential linear programming level-set method for topology optimization*, Structural and Multidisciplinary Optimization, 51 (2015), pp. 631–643.

[18] P. Frey and H. Borouchaki, *Texel: triangulation de surfaces implicites(partie ii, exemples d'applications)*, Rapports de recherche- INRIA, (1997).

[19] A. T. Gaynor and J. K. Guest, *Topology optimization considering overhang constraints: Eliminating sacrificial support material in additive manufacturing through design*, Structural and Multidisciplinary Optimization, 54 (2016), pp. 1157–1172.

[20] I. Gibson, D. W. Rosen, B. Stucker, et al., *Additive manufacturing technologies*, vol. 238, Springer, 2010.

[21] F. Hecht, *New development in freefem++*, Journal of numerical mathematics, 20 (2012), pp. 251–266.

[22] A. Henrot and M. Pierre, *Variation et optimisation de formes: une analyse géométrique*, vol. 48, Springer, 2005.

[23] K. Hu, S. Jin, and C. C. Wang, *Support slimming for single material based additive manufacturing*, Computer-Aided Design, 65 (2015), pp. 1–10.

[24] M. Langelaar, *An additive manufacturing filter for topology optimization of print-ready designs*, Structural and Multidisciplinary Optimization, (2016), pp. 1–13.

[25] M. Langelaar, *Topology optimization of 3d self-supporting structures for additive manufacturing*, Additive Manufacturing, 12 (2016), pp. 60–70.

[26] M. Leary, L. Merli, F. Torti, M. Mazur, and M. Brandt, *Optimal topology for additive manufacture: a method for enabling additive manufacture of support-free optimal structures*, Materials & Design, 63 (2014), pp. 678–690.

[27] F. P. Melchels, M. A. Domingos, T. J. Klein, J. Malda, P. J. Bartolo, and D. W. Hutmacher, *Additive manufacturing of tissues and organs*, Progress in Polymer Science, 37 (2012), pp. 1079–1104.

[28] G. Michailidis, *Manufacturing Constraints and Multi-Phase Shape and Topology Optimization via a Level-Set Method*, PhD thesis, Ecole Polytechnique X, 2014, available at: http://pastel.archives-ouvertes.fr/pastel-00937306.

[29] J. Mireles, D. Espalin, D. Roberson, B. Zinniel, F. Medina, and R. Wicker, *Fused deposition modeling of metals*.

[30] A. M. Mirzendehdel and K. Suresh, *Support structure constrained topology optimization for additive manufacturing*, Computer-Aided Design, 81 (2016), pp. 1–13.

[31] K. Mumtaz, P. Vora, and N. Hopkinson, *A method to eliminate anchors/supports from directly laser melted metal powder bed processes*, in Proc. Solid Freeform Fabrication Symposium, Sheffield, 2011, pp. 55–64.

[32] F. Murat and J. Simon, *Etude de problèmes d'optimal design*, Optimization Techniques Modeling and Optimization in the Service of Man Part 2, (1976), pp. 54–62.
[33] A. Novotny and J. Sokołowski, *Topological Derivatives in Shape Optimization*, Springer, 2013.
[34] S. Osher and R. Fedkiw, *Level set methods and dynamic implicit surfaces*, vol. 153 of Applied Mathematical Sciences, Springer-Verlag, New York, 2003.
[35] S. Osher and J. Sethian, *Fronts propagating with curvature-dependent speed: algorithms based on hamilton-jacobi formulations*, Journal of computational physics, 79 (1988), pp. 12–49.
[36] R. Paul and S. Anand, *Optimization of layered manufacturing process for reducing form errors with minimal support structures*, Journal of Manufacturing Systems, 36 (2015), pp. 231–243.
[37] V. Petrovic, J. Vicente Haro Gonzalez, O. Jorda Ferrando, J. Delgado Gordillo, J. Ramon Blasco Puchades, and L. Portoles Grinan, *Additive layered manufacturing: sectors of industrial application shown through case studies*, International Journal of Production Research, 49 (2011), pp. 1061–1079.
[38] O. Pironneau, *Optimal shape design for elliptic systems*, Springer Series in Computational Physics, Springer-Verlag, New York, 1984.
[39] X. Qian, *Undercut and overhang angle control in topology optimization: a density gradient based integral approach*, International Journal for Numerical Methods in Engineering, (2017).
[40] J. Sethian, *Level set methods and fast marching methods: evolving interfaces in computational geometry, fluid mechanics, computer vision, and materials science*, Cambridge university press, 1999.
[41] J. Sethian and A. Wiegmann, *Structural boundary design via level set and immersed interface methods*, Journal of computational physics, 163 (2000), pp. 489–528.
[42] D. Thomas, *The development of design rules for selective laser melting*, PhD thesis, University of Wales, 2009.
[43] M. Wang, X. Wang, and D. Guo, *A level set method for structural topology optimization*, Computer methods in applied mechanics and engineering, 192 (2003), pp. 227–246.
[44] W. Wang, T. Y. Wang, Z. Yang, L. Liu, X. Tong, W. Tong, J. Deng, F. Chen, and X. Liu, *Cost-effective printing of 3d objects with skin-frame structures*, ACM Transactions on Graphics (TOG), 32 (2013), p. 177.
[45] Y. Wang and Z. Kang, *Structural shape and topology optimization of cast parts using level set method*, International Journal for Numerical Methods in Engineering, (2017).
[46] Y. Zhu, X. Tian, J. Li, and H. Wang, *The anisotropy of laser melting deposition additive manufacturing ti–6.5 al–3.5 mo–1.5 zr–0.3 si titanium alloy*, Materials & Design, 67 (2015), pp. 538–542.